A micro-mechanical model of reinforced polymer failure with length scale effects and predictive capabilities. Validation on carbon fiber reinforced high-crosslinked RTM6 epoxy resin

Van-Dung Nguyen[a], Ling Wu[a], Ludovic Noels[a,*]

[a]*University of Liege, Department of Mechanical and Aerospace Engineering, Computational & Multiscale Mechanics of Materials, Allée de la découverte 9, B-4000 Liège, Belgium*

Abstract

We propose a micro-mechanical numerical model able to predict the nonlinear behavior and failure of unidirectional fiber reinforced high-crosslinked epoxy subjected to transverse loading conditions. Statistical microstructural volume elements (SMVE) of a realistic composite material are generated from the statistical characterization of the fibers distribution and fiber radius estimated from SEM images of a similar material system. The fibers are assumed to be transversely hyperelastic isotropic and the matrix obeys a hyperelastic viscoelastic-viscoplastic constitutive model enhanced by a multi-mechanism nonlocal damage model. This polymer model captures the pressure dependency and strain rate effects. Besides, it also accounts for size effects through its internal length scales, allowing capturing, with the same unique set of parameters, the behaviors of the epoxy as pure material as well as matrix phase in composites, which are experimentally observed to be different. Additionally, since fiber/matrix interfaces of the considered composite material are categorized as strong ones, the true underlying failure mechanism is located in the matrix close to the fibers, and the interface does not need to be explicitly introduced in the model. The model prediction is found to be in good agreement with experimental results in terms of the global nonlinear stress-strain curves over various strain rates and pressure conditions, on the one hand for pure matrix samples, and on the other hand for the composite coupons, making the proposed framework a predictive virtual testing facility for material design. Finally, using this model, we study the localization behavior in order to characterize the post-failure behavior of the composite material: the cohesive strength is given by the stress-strain curve peak stress while the critical energy release rate is estimated by evaluating the dissipated energy accumulated during the post-peak localization stage. Finally, different SMVE realizations are considered allowing assessing the discrepancy in the failure characteristics of composites.

Keywords: Composites, high-crosslinked epoxy, homogenization, length scale effect, failure

1. Introduction

Nowadays, fiber reinforced materials are widely used in various fields of engineering applications because of their exceptional properties. The fabrication and testing of the composites are generally costly and time-consuming. Therefore, numerical methods should be used in order to facilitate and accelerate the evaluation process of a new material. The mechanical behavior, in particular when studying failure, of this kind of material depends on the details of their material microstructure including the mechanical behavior and the complex spatial arrangement of their constituents. Macroscopic cracks generally result from the damage and failure events at the microstructure level, including matrix localization under shear bands, matrix cracking,

---

*Corresponding author, Phone: +32 4 366 48 26, Fax: +32 4 366 95 05
Email addresses: `VanDung.Nguyen@ulg.ac.be` (Van-Dung Nguyen), `L.Wu@ulg.ac.be` (Ling Wu), `L.Noels@ulg.ac.be` (Ludovic Noels)

fiber/matrix decohesion, fiber breaking, and delamination. As a result, the damage and failure modeling of composites requires a multiscale approach incorporating the lower scale mechanisms.

In a homogenization-based multiscale approach, the homogenized properties are estimated from microscale models and are transferred to an upper-scale problem. On the one hand, two-scale homogenization frameworks are accurate tools incorporating directly the material behavior through multiple scales, see the review [1]. In this approach, a finite element (FE) simulation is performed at the macroscale and the constitutive relations at each macroscopic material point of interest (integration point in the context of FE) are estimated "on the fly" from the resolution of a microscale model defined at that point. This two-scale strategy has been considered not only for continuous problems but also for discontinuous problems with evolving damage and failure. In the latter cases, the representativity of the microscale problem is lost during the softening stage and, as a result, the homogenized stress-strain response depends on the dimensions of the microscopic problem: a larger dimension along the loading direction leads to a more pronounced snapback in the stress-strain response. However, the objectivity with the dimensions of the microscopic problems can be recovered, *e.g.* in terms of a homogenized Traction Separation Law (TSL) [2, 3] governing a Cohesize Zone Model (CZM). Although two-scale approaches can be considered for structures made of composites, a simulation still requires a lot of computational resources and computational time, in particular when dealing with the material failure. On the other hand, a numerical homogenization is more attractive from the computational efficiency. This approach assumes a closed form of the homogenized constitutive relations and the microscale models are used to calibrate the underlying constitutive parameters [4]; there is no coupling between the macroscale and microscale problems but the relevant information from microscale simulations is accounted for. The homogenized constitutive relations consist in material responses under the form of strain-stress curves to model the pre-failure stage, but they can also consist in homogenized TSL in order to model the failure onset and crack propagation using CZM [4]. In this case, the TSL combines the material cohesive strength (denoted by σ_c) and fracture energy (denoted by G_c) to describe the resistance of crack lips opening. The shape of the TSL (such as linear, exponential, polynomial, monotonically, *etc.*) is generally postulated since it is less important than σ_c and G_c [5]. However, the two homogenization-based multiscale approaches require an accurate microscale model of the composite material, which is the objective of this paper.

At the microstructure level, among various possible models, computational micromechanics provides an accurate framework allowing directly relating the homogenized material behavior to its microstructure evolution [1]. In case of fiber reinforced composites, this technique can predict the mechanical behavior, including the failure mechanisms under complex loading conditions, as demonstrated by numerous numerical studies [6, 7, 3] and references therein as a non-exhausted list. The finite element (FE) simulations are carried out on statistical microstructural volume elements (SMVE), extracted from the composite microstructure, by considering either single loading modes (tension, compression, and shear) or combined loading modes. The constitutive laws of fibers, matrix and of their interfaces are explicitly introduced. From the computational point of view, computational micromechanics plays as a virtual experiment facility in which a parametric study, including the influence of the constituent properties as well as the microstructure topology, is easily conducted on the mechanical response and the microstructure evolution of the composite material.

However, microscale simulations remain highly challenging. In general each constituent of the composite material, the polymeric matrix in particular, requires a complex material model and the identification of its parameters. One methodology is to test pure polymer samples in order to identify their material parameters, assuming that the polymer behavior is the same as in the composite material. However this assumption is still uncertain [8], and a reverse engineering step is usually conducted to evaluate the polymer response of the composite material matrix, which prevents the models to be predictive. Moreover the microstructure suffers from uncertainty [9], which should be accounted for in the virtual testing. Finally, in order to be able to consider composites failure, since σ_c and G_c are two relevant parameters of the homogenized cohesive laws, they need to be estimated in an efficient and accurate way. The value of σ_c is easily estimated from the stress-strain curve. However, the value of G_c should be estimated by accumulating the dissipated energy during post-peak localization stage. One should note that these two parameters are dependent on the stress-strain state applied to the microscale problem during the virtual test. Therefore, the micromechanics numerical simulations should be carried out with complex mechanisms involving softening and possible snapbacks in

order to extract these relevant parameters, which requires the development of a robust framework under localization.

The objective of this work is to provide an efficient virtual testing facility for carbon fibers/high-crosslinked RTM6 epoxy composites allowing the nonlinear behavior, as well as the material cohesive strength and fracture energy, to be estimated in an predictive way. To this end we aim at addressing the issues that have been pointed out.

The first difficulty addressed in this paper is the modeling of the matrix behavior in the composite material. The mechanical behavior of the high-crosslinked RTM6 epoxy was studied experimentally in [10] with a set of mechanical tests at various levels of triaxiality (such as shear, uniaxial tension, uniaxial compression) as well as of strain rates. Rate-dependent behavior of this epoxy resin can be modeled either by a viscoelastic-viscoplastic model [11], by a viscoplastic-damage model [10] or by a viscoelastic-viscoplastic-nonlocal damage model [12]. This epoxy resin can be used as the matrix of a unidirectional composite of carbon fibers and experimental testing of cubic samples made of this composite was performed under uniaxial compression at various strain rates [8]. The manufacturing of the tested cubic samples was made through a resin transfer molding (RTM) process in order to perfectly replicate the curing conditions of the bulk matrix (high-crosslinked RTM6 epoxy resin) which was considered in [10, 12]. As a result, the constitutive model developed for the RTM6 epoxy resin in [10, 12] could have been used to represent the matrix behavior under the assumption that the responses of the RTM6 epoxy as a bulk material and as a composite material phase are identical. However, using the constitutive model developed and identified by [10] within a composite material leads to FE predictions underestimating the experimental values of the peak stress [8]. An assumption to explain this discrepancy is the existence of a length scale effect in the irreversible behavior of the epoxy [8]. The presence of fibers embedded in the matrix (*e.g.* fiber diameter, fiber spacing) should be included in the constitutive relation of the matrix by a material length scale. The constitutive model developed in [12] allows incorporating such a length scale. In this work, we will show that, because of this length scale, a unique set of material parameters allows modeling the pure resin behavior and the composite material response in good agreement with the corresponding experimental measurements, making the numerical framework predictive.

The second point addressed in the work is to carry out numerical tests on the SMVEs representative of a real microstructure: the sizes and spatial distribution of carbon fibers must closely correspond to the ones of the real microstructure. Most of available numerical studies have made the assumption of a periodic fiber arrangement in the matrix, see *e.g* [13] for generating periodic and random SMVEs. However this periodic assumption acts as a constraint of the microstructure generator and makes the distribution of the fibers far from the real one: the real microstructure of composites possesses a high irregular dispersion of fibers, which has a significant effect on the failure/damage initiation and evolution under certain loading conditions. In this work, statistically equivalent random microstructures are generated using the statistical information of real microstructures [9].

The third difficulty addressed in this paper is to model the composite material post-softening response. The transverse failure mode (including matrix failure and fiber/matrix debonding) is often considered as the first failure mechanism which leads to the deviation of the material behavior from linear elasticity. Transverse tensile loading results in the matrix cracking and/or fiber/matrix debonding [14] while the failure under transverse compressive loading is controlled by the localization of the matrix plastic strain along shear bands; interface decohesion develops afterwards around these bands; and final fracture occurs by matrix cracking [6]. However, the failure scenario at matrix/fiber interfaces is not clear by the fact that the true failure mechanism can be either due to the failure of the interfacial bonding or to the failure of the matrix close to the fiber (so-called interphase). From the experimental tests performed by [14] on composites with weak and strong fiber/matrix interfaces, the SEM results show that the dominating failure mechanism in case of a weak interface is a true interfacial failure while in case of a strong interface the dominating failure mechanism is an interphase failure. Strong interfaces lead to a very small number of isolated interfacial cracks occurring at each fiber before the sudden ply failure occurs transversely. In contrast, many interfacial cracks grow and connect to a macroscopic crack when the load is increased in the case of weak interfaces [14]. After ultimate fracture, fibers surfaces are observed to be almost totally covered by the matrix in the interphase failure whereas neat carbon fibers are observed in the interfacial

failure. Clearly, in composites with weak interfaces, the fiber/matrix debonding must be explicitly modeled to correctly capture the initiation and propagation of micro-cracks. In composites with strong interfaces, because the true failure mechanism is the matrix cracking, the failure of the matrix and of interfaces is taken into account using a damageable constitutive model for the matrix so that fiber/matrix debonding does not need to be explicitly modeled. Since the fiber/matrix interfaces of the considered composite material is categorized into the strong ones [14], they are not explicitly modeled and it will be demonstrated that the damageable matrix model developed in [12] can capture the failure pattern. However, in order to conduct the simulations, the numerical framework ought to be developed in a robust way able to capture local and global softening, as well as snapback behaviors. The finite element resolution of the boundary value problem, defined by the SMVE geometry, the constituents material behaviors, and the boundary condition, follows a standard procedure based on an incremental Newton-Raphson iterative scheme. Nevertheless, on the one hand, an incremental control purely based on monotonically increasing the external load cannot pass the limit point, and, on the other hand, an incremental control purely based on prescribed displacements cannot follow a snap-back unstable behavior. To overcome these problems, the path following technique based on dissipation constraint [15] is extended in this work to account for the physical nonlinearities due to high strain localization.

The paper is organized as follows. The constitutive models of fibers and matrix are described in Section 2. Section 3 presents the computational framework of the virtual test. In particular, the nonlinear subscale boundary value problem is detailed with its corresponding boundary conditions and the extraction of the material strength and fracture energy. Identification of the material parameters and experimental validation are conducted in Section 4 for several loading strain rates and pressure conditions. Finally, the material strength and the critical energy release rate of the considered composite material are extracted in Section 5.

2. Constitutive models

This section presents briefly the constitutive laws used to describe the behavior of the fiber and matrix phases in fiber reinforced composites. The constitutive models are formulated in large strains using the total Lagrange formulation. The material point $\mathbf{x}$ in the deformed configuration is characterized by a two-point mapping $\mathbf{x} = \mathbf{x}(\mathbf{X}, t)$ where $\mathbf{X}$ is its reference location in the undeformed configuration. This mapping leads to the definition of the deformation gradient tensor $\mathbf{F}$

$$\mathbf{F} = \mathbf{x} \otimes \boldsymbol{\nabla}_0 = \mathbf{I} + \mathbf{u} \otimes \boldsymbol{\nabla}_0, \tag{1}$$

where $\mathbf{u} = \mathbf{x} - \mathbf{X}$ denotes the displacement vector. The stress measure is the first Piola-Kirchhoff stress tensor $\mathbf{P}$, which is energetically conjugate to $\mathbf{F}$. While the fibers are considered as a transversely isotropic and linear elastic material [3], the matrix obeys the multi-mechanism nonlocal damage model proposed in [12]. The interfaces between matrix and fibers are assumed to be perfectly coherent.

2.1. Fiber phase

When considering transverse mechanical behavior of the unidirectional fibers reinforced composites, an isotropic elastic model is generally assumed for the fibers since only the plane strain deformation mode is considered, see *e.g.* [7]. In that case, the transverse Young's modulus of the fibers should be used. In this work, a general large strain hyperelastic model is applied with a view toward general three-dimensional simulations, see *e.g.* [3].

The fibers follow a transversely isotropic hyperelastic model characterized by a neo-Hookean strain energy $\Psi_f = \Psi_f(\mathbf{C})$, where the $\mathbf{C} = \mathbf{F}^T \cdot \mathbf{F}$ is the right Cauchy-Green tensor. Considering the transversely isotropic properties of the fibers, Ψ_f can be decomposed into two parts such as

$$\Psi_f = \Psi_f^{\text{iso}} + \Psi_f^{\text{trn}}, \tag{2}$$

where Ψ_f^{iso} and Ψ_f^{trn} are respectively the isotropic and transverse components.

4

A transversely isotropic elastic material is characterized by the following parameters:

$$E_\mathrm{T} = E_1 = E_2 \neq E_3 = E_\mathrm{L}; \qquad \nu_\mathrm{TT} = \nu_{12} = \nu_{21} \neq \nu_{13} = \nu_{23} = \nu_\mathrm{TL};$$
$$G_\mathrm{LT} = G_{13} = G_{23} = G_3; \qquad G_\mathrm{TT} = G_{12} = \tfrac{E_\mathrm{T}}{2(1+\nu_\mathrm{TT})}, \tag{3}$$

where the subscript "3" refers to the fiber direction. Along this direction, the Poisson's ratios are not symmetric but instead satisfy $\nu_{ij}/E_i = \nu_{ji}/E_j$ (no sums).

The isotropic energy part is a function of $\mathbf{C}$ as

$$\Psi_f^\mathrm{iso} = \frac{1}{2} G_{12} \left(I_1 - 3\right) - G_{12} \log J + \frac{1}{2} \lambda \log^2 J, \tag{4}$$

where $I_1 = \operatorname{tr} \mathbf{C}$, $J = \sqrt{\det \mathbf{C}} = \det \mathbf{F}$, and G_{12} and λ are material constants. The transverse energy part is obtained from a generalization of the model proposed by [16]

$$\Psi_f^{trn} = [\alpha_\mathrm{trn} + 2\beta_\mathrm{trn}\ln J + \gamma_\mathrm{trn}(I_4 - 1)](I_4 - 1) - \frac{1}{2}\alpha_\mathrm{trn}(I_5 - 1), \tag{5}$$

where I_4 and I_5 are respectively defined by

$$I_4 = \boldsymbol{A} \cdot \mathbf{C} \cdot \boldsymbol{A} \ \ \text{and} \ \ I_5 = \boldsymbol{A} \cdot \mathbf{C}^2 \cdot \boldsymbol{A}, \tag{6}$$

with the unit vector $\boldsymbol{A}$ defining the main direction of orthotropy (fibers direction) in the undeformed configuration and where α_trn, β_trn, and γ_trn are material constants. The model parameters of Eqs. (4) and (5) are λ, G_{12}, α_trn, β_trn, and γ_trn and follow from the measured properties (3) as

$$
\begin{aligned}
\lambda &= \frac{E_\mathrm{T}\left(\nu_\mathrm{TT} + n\nu_\mathrm{TL}^2\right)}{m\left(1 + \nu_\mathrm{TT}\right)}, \ \ G_{12} = \frac{E_\mathrm{T}}{2\left(1 + \nu_\mathrm{TT}\right)}, \\
\alpha_\mathrm{trn} &= G_{12} - G_3, \\
\beta_\mathrm{trn} &= \frac{E_\mathrm{T}\left[n\nu_\mathrm{TL}\left(1 + \nu_\mathrm{TT} - \nu_\mathrm{TL}\right) - \nu_\mathrm{TT}\right]}{4m\left(1 + \nu_\mathrm{TT}\right)}, \\
\gamma_\mathrm{trn} &= \frac{E_\mathrm{L}\left(1 - \nu_\mathrm{TT}\right)}{8m} - \frac{\lambda + 2G_{12}}{8} + \frac{\alpha_\mathrm{trn}}{2} - \beta_\mathrm{trn}, \\
m &= 1 - \nu_\mathrm{TT} - 2n\nu_\mathrm{TL}^2, \ \ \text{and} \ n = \frac{E_\mathrm{L}}{E_\mathrm{T}}.
\end{aligned}
\tag{7}
$$

The first Piola-Kirchhoff stress tensor can be estimated from the strain energy given by Eq. (2) by

$$
\begin{aligned}
\mathbf{P} = \frac{\partial \Psi_f}{\partial \mathbf{F}} = 2\mathbf{F} \cdot \frac{\partial \Psi_f}{\partial \mathbf{C}} \ = \ & 2\mathbf{F} \cdot \{\lambda\ln J\mathbf{C}^{-1} + G_{12}(\mathbf{I} - \mathbf{C}^{-1}) + 2\beta_\mathrm{trn}(I_4 - 1)\mathbf{C}^{-1} + 2[\alpha_\mathrm{trn} + 2\beta_\mathrm{trn}\ln J + \\
& 2\gamma_\mathrm{trn}(I_4 - 1)]\boldsymbol{A} \otimes \boldsymbol{A} - \alpha_\mathrm{trn}(\mathbf{C} \cdot \boldsymbol{A} \otimes \boldsymbol{A} + \boldsymbol{A} \otimes \mathbf{C} \cdot \boldsymbol{A})\}.
\end{aligned}
\tag{8}
$$

2.2. Matrix phase

The matrix, *e.g.* epoxy, exhibits rate-, time-, pressure-, and temperature-dependent mechanical response [10]. Under uniaxial compressive loading, the whole stress-strain curve can be divided into multiple stages, see Fig. 1a. After an elastic stage at small strains, a prepeak nonlinear stage continues until reaching a peak stress. After this peak value, the stress tends to decrease with increasing deformation. This effect is called softening. At large strains, when the softening is saturated, a rehardening stage takes place. After the onset of failure, the failure stage sets in until reaching total failure. Under uniaxial tensile loading, the rehardening stage is not present as the failure stage follows the peak stress. In order to capture the multi-stage behavior reported in Fig. 1a, the hyperelastic viscoelastic-viscoplastic material law enhanced by a multi-mechanism
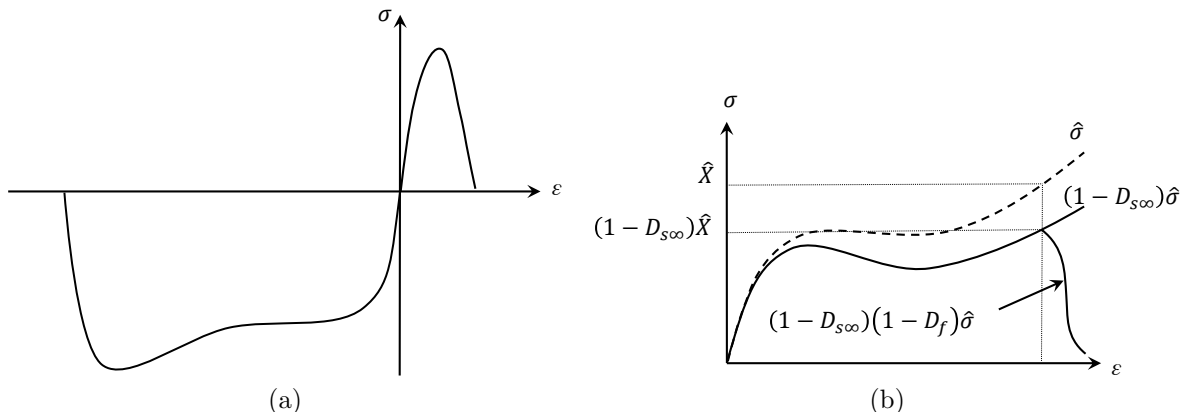
Figure 1: (a) Typical stress-strain curve of amorphous glassy polymers under uniaxial compressive and tensile loading conditions at a constant strain rate [10]; and (b) Modeling strategy [12].

damage model proposed in [12] is used. In this work, the ability of the constitutive model developed in [12] to capture size effects in composites will be demonstrated. Since the details of the model can be found in [12], only its key features are recalled in this section.

The softening and failure phenomena are addressed in the context of the continuum damage mechanics [17]. Under the assumption that the strain measure in the current configuration and in its undamaged representation are equivalent, the first Piola-Kirchhoff stress $\mathbf{P}$ is given by

$$\mathbf{P} = (1 - D)\,\hat{\mathbf{P}}\,, \tag{9}$$

where D is the damage variable which is equal to 0 for intact materials and to 1 when the full failure occurs, and where $\hat{\mathbf{P}}$ denotes the first Piola-Kirchhoff stress tensor in the undamaged representation, so-called the effective first Piola-Kirchhoff stress tensor, which is determined from a hyperelastic potential $\hat{\Psi}$ such as

$$\hat{\mathbf{P}} = \frac{\partial \hat{\Psi}_m}{\partial \mathbf{F}}\,. \tag{10}$$

The modeling strategy to capture the multi-stage behavior reported in Fig. 1a. is schematically demonstrated in Fig. 1b. From the undamaged stress-strain law $\hat{\sigma} = \hat{\sigma}(\varepsilon)$, the softening stage is modeled using a softening variable, denoted by D_s, whose evolution obeys a saturation law, which tends to a saturation value $D_{s\infty}$ when strains increase. When D_s is saturated, the rehardening stage sets in since the hardening of the undamaged part is still developing. After the onset of failure is detected by a failure criterion, the stress decrease is modeled using a failure variable, denoted by D_f. The value of D_f ranges from 0 at the onset of failure to 1 when final failure occurs. Finally, since two distinct softening variables (D_s and D_f) are used, the damage variable D is expressed by

$$D = 1 - (1 - D_s)(1 - D_f)\,. \tag{11}$$

In the following, the viscoelastic-viscoplastic constitutive law specified in Eq. (10) is first briefly recalled. Then the evolution laws for the softening and failure variables are provided. The fully implicit integration scheme of this elasto-visco-plastic constitutive law can be found in [12].

2.2.1. Viscoelastic-viscoplastic constitutive model

Following the standard decomposition in elastoplastic materials at finite strains, the deformation gradient tensor $\mathbf{F}$ is decomposed into a recoverable viscoelastic part, denoted by $\mathbf{F}^{ve}$ and an irrecoverable viscoplastic

part, denoted by $\mathbf{F}^{vp}$ such that

$$\mathbf{F} = \mathbf{F}^{ve} \cdot \mathbf{F}^{vp} \,. \tag{12}$$

The viscoelastic effect is captured using a viscoelastic potential based on the generalized Maxwell model. After some mathematical manipulations, see [12] for details, the effective constitutive relation following Eq. (10) is expressed by

$$\hat{\mathbf{P}} = \mathbf{F}^{ve} \cdot \left(\hat{\boldsymbol{\tau}} : \frac{\partial \ln \mathbf{C}^{ve}}{\partial \mathbf{C}^{ve}} \right) \cdot \mathbf{F}^{vp-T} \,, \tag{13}$$

where $\hat{\boldsymbol{\tau}} = \partial \hat{\Psi}_m / \partial \mathbf{E}^{ve}$ is the stress measure energetically conjugated to the viscoelastic logarithmic strain tensor $\mathbf{E}^{ve} = \ln \sqrt{\mathbf{F}^{veT} \cdot \mathbf{F}^{ve}}$, so-called the corotational Kirchhoff stress

$$\hat{\boldsymbol{\tau}}(t) = \int_{-\infty}^{t} \mathbb{C}^{ve}(t-s) : \frac{\partial \mathbf{E}^{ve}(s)}{\partial s} \, ds \,, \tag{14}$$

with

$$\mathbb{C}^{ve}(t) = 2G(t) \left(\mathcal{I} - \frac{1}{3}\mathbf{I} \otimes \mathbf{I} \right) + K(t)\mathbf{I} \otimes \mathbf{I} \,. \tag{15}$$

In this last equation, $\mathbf{I}$ and $\mathcal{I}$ are respectively the second and the fourth order symmetric identity tensors; $G(t)$ and $K(t)$ are respectively the shear and bulk relaxation functions, which are expressed using Prony series

$$G(t) = G_\infty + \sum_{i=1}^{N} G_i \exp\left(-\frac{t}{g_i}\right) \,, \text{ and } K(t) = K_\infty + \sum_{i=1}^{N} K_i \exp\left(-\frac{t}{k_i}\right) \,, \tag{16}$$

where g_i and k_i, with $i = 1, \ldots, N$, are the shear and volumetric relaxation times; G_i and K_i, with $i = 1, \ldots, N$, are the shear and bulk moduli, and G_∞ and K_∞ are the permanent elastic shear and bulk moduli.

The viscoplastic flow is modeled using the Perzyna-type viscoplastic flow rule [18], which can be expressed by the following relation

$$\mathbf{D}^{vp} = \dot{\mathbf{F}}^{vp} \cdot \mathbf{F}^{vp-1} = \frac{1}{\eta} \langle F \rangle^{\frac{1}{p}} \frac{\partial P}{\partial \hat{\boldsymbol{\tau}}} \,, \tag{17}$$

where $\mathbf{D}^p$ is the viscoplastic strain rate, F is the yield function, P is the flow potential, η is the viscosity, p is the rate sensitivity exponent, and $\langle F \rangle = (F + |F|)/2$. Clearly, if $F \leq 0$, plastic flow does not occur since $\mathbf{D}^p = 0$. The yield function F and the plastic potential P are given as follows

$$F = \left(\frac{\phi_{eq}}{\sigma_c} \right)^\alpha - \frac{m^\alpha - 1}{m+1} \frac{\operatorname{tr}\boldsymbol{\phi}}{\sigma_c} - \frac{m^\alpha + m}{m+1} \,, \tag{18}$$

$$P = \phi_{eq}^2 + \beta \left(\frac{\operatorname{tr}\boldsymbol{\phi}}{3} \right)^2 \,, \text{ and}$$

$$\phi_{eq} = \sqrt{\frac{3}{2}\operatorname{dev}\boldsymbol{\phi} : \operatorname{dev}\boldsymbol{\phi}} \,, \operatorname{tr}\boldsymbol{\phi} = \phi_{ii} \,, m = \frac{\sigma_t}{\sigma_c} \,,$$

where $\boldsymbol{\phi} = \hat{\boldsymbol{\tau}} - \hat{\mathbf{b}}$ is the combined stress tensor; $\hat{\mathbf{b}}$ is the backstress tensor defined to capture the re-hardening effect; σ_c and σ_t are the isotropic compressive and tensile yield stresses respectively; m is the tensile/compression yield anisotropy; and α and β are material constants.

The hardening effects are introduced through the evolutions of the isotropic compressive hardening stress σ_c, the isotropic tensile hardening stress σ_t, and the backstress tensor $\hat{\mathbf{b}}$ with respect to the plastic

deformation state. From the viscoplastic deformation tensor specified in Eq. (17), the equivalent plastic strain is defined by

$$\dot{\gamma} = \frac{1}{\sqrt{1 + 2\nu_p^2}} \sqrt{\mathbf{D}^p : \mathbf{D}^p} \,, \tag{19}$$

where ν_p is the initial plastic Poisson's ratio, which relates to the parameter β used in the flow potential in Eqs. (18), with

$$\nu_p = \frac{9 - 2\beta}{18 + 2\beta} \,. \tag{20}$$

The hardening evolution laws are given by

$$\dot{\hat{\mathbf{b}}} = H_b(\gamma) \mathbf{D}^{vp} \,, \dot{\sigma}_c = H_c(\gamma) \dot{\gamma} \,, \text{and } \dot{\sigma}_t = H_t(\gamma) \dot{\gamma} \,, \tag{21}$$

with the initial conditions $\hat{\mathbf{b}}(\gamma = 0) = 0$, $\sigma_c(\gamma = 0) = \sigma_c^0$, and $\sigma_t(\gamma = 0) = \sigma_t^0$. In the last equations, H_b, H_c, and H_t are respectively the kinematic, isotropic compressive, and isotropic tensile hardening moduli, and σ_c^0 and σ_t^0 are respectively the initial yielding compressive and tensile stresses.

2.2.2. Softening model

The phenomenological softening variable D_s is introduced to capture the softening effect. Therefore the evolution of D_s obeys a saturation law, and tends to its saturated value $D_{s\infty}$ (with $D_{s\infty} < 1$) when strains increase. Following [12], this saturation law is given under an explicit form

$$\dot{D}_s = H_s (\chi_s - \chi_{s0})^{\zeta_s} (D_{s\infty} - D_s) \dot{\chi}_s \,, \text{ and}$$
$$\chi_s(t) = \max(\chi_{s0}, \bar{\gamma}(\tau); \tau \in [0 \; t]) \,, \tag{22}$$

where H_s, ζ_s, and $D_{s\infty}$ are material constants, where χ_{s0} is the onset of the softening stage, and where $\bar{\gamma}$ is the nonlocal plastic strain, which is estimated from a Helmholtz-type equation [19]

$$\bar{\gamma} - \boldsymbol{\nabla}_0 \cdot c_s \boldsymbol{\nabla}_0 \bar{\gamma} = \gamma \,, \tag{23}$$

in order to overcome the issue of mesh dependency that appears with local damage models [19]. In the last equation, c_s is the square of the softening nonlocal length scale. This intrinsic length allows interactions between neighboring material points, so that not only this mesh-dependency numerical deficiency is resolved but the size effect observed during this stage can also be captured. Equation (22) can be integrated, leading to

$$D_s = D_{s\infty} \left\{ 1 - \exp\left(-\frac{H_s}{\zeta_s + 1} (\chi_s - \chi_{s0})^{\zeta_s + 1} \right) \right\} \,. \tag{24}$$

2.2.3. Failure model

The onset of failure is detected through a pressure-dependent failure criterion in order to capture the pressure sensitivity process. Since in this work we are interested in a high-crosslinked epoxy matrix, instead of using a stress-based criterion as considered in [12], a criterion of the failure onset based on the equivalent plastic strain should be used [10], with the general form

$$\Phi_f = \gamma - a \exp(-bT) - c = 0 \,, \tag{25}$$

where the stress triaxiality is estimated by $T = \frac{\text{tr} \hat{\boldsymbol{\tau}}}{3\hat{\tau}_{eq}}$, with $\hat{\tau}_{eq} = \sqrt{\frac{3}{2} \text{dev} \hat{\boldsymbol{\tau}} : \text{dev} \hat{\boldsymbol{\tau}}}$, and where a, b, and c are material constants. After the onset of failure defined by Eq. (25), the evolution of the failure surface follows

the Kuhn-Tucker condition

$$\Phi_f - r \le 0 \,, \quad \dot{r} \ge 0 \,, \text{ and } \quad \dot{r}\left(\Phi_f - r\right) = 0 \,, \tag{26}$$

where r is a non-negative variable, whose initial value is equal to 0, introduced to follow the maximal failure criterion ever reached in the loading loading history. Equation (26) allows defining the failure plastic strain, denoted by γ_f, whose evolution is estimated by

$$\dot{\gamma}_f = \begin{cases} 0 & \text{if } \dot{r} = 0 \,, \\ \dot{\gamma} & \text{if } \dot{r} > 0 \,. \end{cases} \tag{27}$$

The failure variable D_f is driven by the nonlocal failure plastic strain following

$$\dot{D}_f = H_f \left(\chi_f\right)^{\zeta_f} \left(1 - D_f\right)^{-\zeta_d} \dot{\chi}_f \,, \text{ and} \tag{28}$$
$$\chi_f(t) = \max\left(\bar{\gamma}_f(\tau)\,; \tau \in [0\ t]\right),$$

where $H_f > 0$, $\zeta_f > 0$, and $\zeta_d > 0$ are material constants and where $\bar{\gamma}_f$ is the nonlocal failure plastic strain, which is estimated from another Helmholtz-type equation [19]

$$\bar{\gamma}_f - \boldsymbol{\nabla}_0 \cdot c_f \boldsymbol{\nabla}_0 \bar{\gamma}_f = \gamma_f \,. \tag{29}$$

In this last equation, c_f is the square of failure nonlocal length scale, which is also introduced in order to overcome the issue of mesh dependency. This intrinsic length allows resolving the loss of ellipticity of the boundary value problem and its susceptibility to size effects. Equation (28) can be integrated, leading to

$$D_f = 1 - \left[1 - \left(\frac{\chi_f}{\chi_{fc}}\right)^{\zeta_f + 1}\right]^{\frac{1}{\zeta_d + 1}} \,, \tag{30}$$

where χ_{fc} is the critical nonlocal failure plastic strain, which satisfies $D_f\left(\chi_f = \chi_{fc}\right) = 1$ and is related to the other constants by

$$\chi_{fc} = \left(\frac{1}{H_f} \frac{\zeta_f + 1}{\zeta_d + 1}\right)^{\frac{1}{\zeta_f + 1}} \,. \tag{31}$$

When $\chi_f \ge \chi_{fc}$ the material is completely damaged and the integration point should be removed from computation since its load capacity no longer exists possibly leading to convergence issues. To avoid this problem, a smooth function $\chi_f^* = \chi_f^*\left(\chi_f\right)$ is considered for the nonlocal failure plasticity such that Eq. (30) can be rewritten as

$$D_f = 1 - \left[1 - \left(\frac{\chi_f^*}{\chi_{fc}}\right)^{\zeta_f + 1}\right]^{\frac{1}{\zeta_d + 1}} \,, \tag{32}$$

where

$$\chi_f^* = \begin{cases} \chi_f & \text{if } \chi_f \le \chi_{fc}^* \,, \\ \chi_{fc}^* + \left(\chi_{fc} - \chi_{fc}^*\right)\left[1 - \exp\left(-\frac{\chi_f - \chi_{fc}^*}{\chi_{fc} - \chi_{fc}^*}\right)\right] & \text{if } \chi_{fc}^* < \chi_f \,. \end{cases} \tag{33}$$

In the last equation, χ_{fc}^* is the onset value of the smooth stage. In this work, a fixed $\chi_{fc}^* = 0.8\chi_{fc}$ is used.

2.3. Dissipated energy

At an arbitrary material point, the total internal power is given at time t by $\mathbf{P} : \dot{\mathbf{F}}$. The reversible part of the internal power at time t is determined by $\dot{\Psi}$ where Ψ is the hyperelastic potential. The dissipated

part denoted by $\dot{\Upsilon}$ is then estimated by

$$\dot{\Upsilon} = \mathbf{P} : \dot{\mathbf{F}} - \dot{\Psi} \,. \tag{34}$$

Following the second law of thermodynamics, the Clausius-Duhem inequality $\dot{\Upsilon} \geq 0$ must be satisfied.

The fibers are modeled as a purely elastic behavior, so that $\dot{\Upsilon}_f = 0$. For the matrix, the dissipated rate is given by

$$\dot{\Upsilon}_m = \mathbf{P} : \dot{\mathbf{F}} - \dot{\Psi}_m \,, \tag{35}$$

where Ψ_m is the elastic potential, which is estimated from its undamaged counterpart $\hat{\Psi}_m$ following Eq. (10), with, at a given damage state D,

$$\Psi_m = (1 - D)\, \hat{\Psi}_m \,. \tag{36}$$

The multiplicative decomposition (12) leads to $\dot{\mathbf{F}} = \dot{\mathbf{F}}^{ve} \cdot \mathbf{F}^{vp} + \mathbf{F}^{ve} \cdot \dot{\mathbf{F}}^{vp}$ from which Eq. (35) can be rewritten as

$$\dot{\Upsilon}_m = \mathbf{P} : \left(\dot{\mathbf{F}}^{ve} \cdot \mathbf{F}^{vp} \right) + \mathbf{P} : \left(\mathbf{F}^{ve} \cdot \dot{\mathbf{F}}^{vp} \right) - (1 - D)\, \dot{\hat{\Psi}}_m + \hat{\Psi}_m \dot{D} \,, \tag{37}$$

in which $\dot{\Psi}_m = (1 - D)\, \dot{\hat{\Psi}}_m - \hat{\Psi}_m \dot{D}$ is used following Eq. (36). Since following Eqs. (9, 10) $\mathbf{P} : \left(\dot{\mathbf{F}}^{ve} \cdot \mathbf{F}^{vp} \right) = (1 - D)\, \dot{\hat{\Psi}}_m$, Eq. (37) can be rewritten as

$$\dot{\Upsilon}_m = \mathbf{P} : \left(\mathbf{F}^{ve} \cdot \dot{\mathbf{F}}^{vp} \right) + \hat{\Psi}_m \dot{D} \,. \tag{38}$$

This equation shows that the dissipated energy results from plastic deformation and from the damage evolution. From the definition of the effective corotational stress following Eq. (13), this last equation is eventually rewritten as

$$\dot{\Upsilon}_m = (1 - D)\, \hat{\boldsymbol{\tau}} : \mathbf{D}^{vp} + \hat{\Psi}_m \dot{D} \,. \tag{39}$$
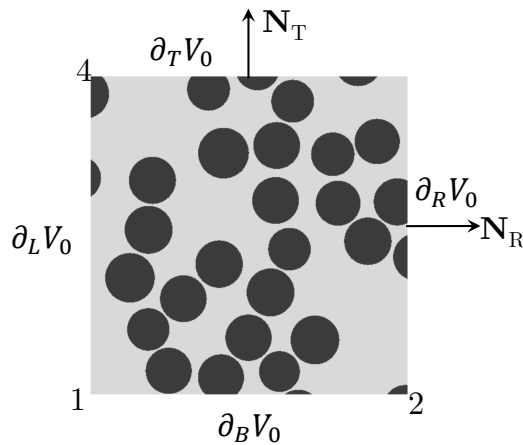
3. Computational framework

Figure 2: A typical microscopic volume element for virtual test with boundary parts $\partial V_0 = \partial_L V_0 \cup \partial_R V_0 \cup \partial_T V_0 \cup \partial_B V_0$ and control nodes 1, 2, and 4. Two unit vectors $\mathbf{N}_R$ and $\mathbf{N}_T$ normal to $\partial_R V_0$ and $\partial_T V_0$, respectively, are also shown.

The basic of computational micromechanics is to evaluate the homogenized response for a specific loading path by resolving a microscale boundary value problem. This section provides a virtual experiment testing methodology using the constitutive models presented in Section 2 to predict the homogenized behavior of fiber reinforced composites. Since we are interested in unidirectional composites, two-dimensional problems are considered but the strategy can be extended to three-dimensional cases. A rectangular SMVE denoted by V_0 is considered, see Fig. 2. Its external boundary ∂V_0 can be divided into 4 non-overlapping parts, with $\partial V_0 = \partial_L V_0 \cup \partial_R V_0 \cup \partial_T V_0 \cup \partial_B V_0$, which are distinct at the 4 corner nodes. The set of interfaces between the fiber and the matrix, so-called internal boundary, is denoted by $\partial_I V_0$. One can also define $\mathbf{N}$ as the outward reference unit normal vector and $\mathbf{N}^I$ as the reference unit normal vector of $\partial_I V_0$, which is oriented from the fiber to the matrix.

3.1. Microscopic boundary value problem with multiple nonlocal variables

Because of the constitutive law of the matrix material, which is modeled with the multiple-mechanism nonlocal damage model, the microscopic BVP follows a multi-variable nonlocal continuum where the nonlocal equations (23, 29) must be simultaneously solved with the equilibrium stress equation. In the absence of body forces, the local strong form is given by the following system of equations

$$\begin{cases} \mathbf{P} \cdot \boldsymbol{\nabla}_0 = \mathbf{0} \\ \bar{\gamma} - \boldsymbol{\nabla}_0 \cdot c_s \boldsymbol{\nabla}_0 \bar{\gamma} = \gamma \qquad \text{on } V_0 \,. \\ \bar{\gamma}_f - \boldsymbol{\nabla}_0 \cdot c_f \boldsymbol{\nabla}_0 \bar{\gamma}_f = \gamma_f \end{cases} \tag{40}$$

The weak form of the strong form (40) is stated as finding $(\mathbf{u}, \bar{\gamma}, \bar{\gamma}_f)$ such that

$$\begin{cases} \langle \dot{\mathbf{u}} \cdot (\mathbf{P} \cdot \boldsymbol{\nabla}_0) \rangle_{V_0} = 0 \\ \langle (\bar{\gamma} - \boldsymbol{\nabla}_0 \cdot c_s \boldsymbol{\nabla}_0 \bar{\gamma} - \gamma) \dot{\bar{\gamma}} \rangle_{V_0} = 0 \qquad \forall (\dot{\mathbf{u}}, \dot{\bar{\gamma}}, \dot{\bar{\gamma}}_f) \text{ kinematically admissible}\,. \\ \langle (\bar{\gamma}_f - \boldsymbol{\nabla}_0 \cdot c_f \boldsymbol{\nabla}_0 \bar{\gamma}_f - \gamma_f) \dot{\bar{\gamma}}_f \rangle_{V_0} = 0 \end{cases} \tag{41}$$

In these last equations, $\langle \bullet \rangle_{V_0}$ is the volume averaging operator over the SMVE, with

$$\langle \bullet \rangle_{V_0} = \frac{1}{|V_0|} \int_{V_0} \bullet \, dV \,, \tag{42}$$

where $\bullet$ represents an arbitrary quantity and where $|V_0|$ denotes the volume measure of the domain V_0.

By applying the integration by parts and Gauss' theorem, the weak form (41) can be rewritten as

$$\begin{cases} \langle \mathbf{P} : (\dot{\mathbf{u}} \otimes \boldsymbol{\nabla}_0) \rangle_{V_0} - \frac{1}{|V_0|} \int_{\partial V_0} \dot{\mathbf{u}} \cdot \mathbf{T} \, dA = 0 \\ \langle (\bar{\gamma} - \gamma) \dot{\bar{\gamma}} + c_s \boldsymbol{\nabla}_0 \bar{\gamma} \cdot \boldsymbol{\nabla}_0 \dot{\bar{\gamma}} \rangle_{V_0} - \frac{1}{|V_0|} \int_{\partial V_0} c_s \boldsymbol{\nabla}_0 \bar{\gamma} \cdot \mathbf{N} \dot{\bar{\gamma}} \, dA + \frac{1}{|V_0|} \int_{\partial_I V_0} [\![c_s \boldsymbol{\nabla}_0 \bar{\gamma} \dot{\bar{\gamma}}]\!] \cdot \mathbf{N}^I \, dA = 0 \,, \\ \langle (\bar{\gamma}_f - \gamma_f) \dot{\bar{\gamma}}_f + c_f \boldsymbol{\nabla}_0 \bar{\gamma}_f \cdot \boldsymbol{\nabla}_0 \dot{\bar{\gamma}}_f \rangle_{V_0} - \frac{1}{|V_0|} \int_{\partial V_0} c_f \boldsymbol{\nabla}_0 \bar{\gamma}_f \cdot \mathbf{N} \dot{\bar{\gamma}}_f \, dA + \frac{1}{|V_0|} \int_{\partial_I V_0} [\![c_f \boldsymbol{\nabla}_0 \bar{\gamma}_f \dot{\bar{\gamma}}_f]\!] \cdot \mathbf{N}^I \, dA = 0 \,, \end{cases} \tag{43}$$

where $\mathbf{T}$ is the traction vector per unit reference surface of ∂V_0

$$\mathbf{T} = \mathbf{P} \cdot \mathbf{N}\,, \tag{44}$$

and where $[\![\bullet]\!]$ and $\langle \bullet \rangle$ are respectively the jump and mean operators defined at the interface between fibers and matrix with

$$\begin{cases} [\![\bullet]\!] = \bullet_{\text{matrix}} - \bullet_{\text{fiber}} \,, \\ \langle \bullet \rangle = \frac{1}{2} (\bullet_{\text{matrix}} + \bullet_{\text{fiber}}) \,. \end{cases} \tag{45}$$

From the weak form (43), the boundary conditions must be defined not only for the displacement field $\mathbf{u}$ but also for nonlocal variables $\bar{\gamma}$ and $\bar{\gamma}_f$, especially those at the fiber/matrix interfaces. In principle, the

boundary conditions for nonlocal variables are introduced at ∂V_0 and $\partial_I V_0$ in such a way that the following equations are *a priori* satisfied [20]

$$\begin{cases} \int_{\partial V_0} c_s \boldsymbol{\nabla}_0 \bar{\gamma} \cdot \mathbf{N} \dot{\bar{\gamma}} \, dA = 0 \,, \\ \int_{\partial V_0} c_f \boldsymbol{\nabla}_0 \bar{\gamma}_f \cdot \mathbf{N} \dot{\bar{\gamma}}_f \, dA = 0 \,, \\ \int_{\partial_I V_0} [\![c_s \boldsymbol{\nabla}_0 \bar{\gamma} \dot{\bar{\gamma}}]\!] \cdot \mathbf{N}^I \, dA = 0 \,, \\ \int_{\partial_I V_0} [\![c_f \boldsymbol{\nabla}_0 \bar{\gamma}_f \dot{\bar{\gamma}}_f]\!] \cdot \mathbf{N}^I \, dA = 0 \,. \end{cases} \tag{46}$$

The details of these boundary conditions are discussed in Section 3.4. With the boundary conditions specified in Eqs. (46), the weak form (43) is written under the simpler form

$$\begin{cases} \langle \mathbf{P} : (\dot{\mathbf{u}} \otimes \boldsymbol{\nabla}_0) \rangle_{V_0} - \frac{1}{|V_0|} \int_{\partial V_0} \dot{\mathbf{u}} \cdot \mathbf{T} \, dA = 0 \,, \\ \langle (\bar{\gamma} - \gamma) \dot{\bar{\gamma}} + c_s \boldsymbol{\nabla}_0 \bar{\gamma} \cdot \boldsymbol{\nabla}_0 \dot{\bar{\gamma}} \rangle_{V_0} = 0 \,, \\ \langle (\bar{\gamma}_f - \gamma_f) \dot{\bar{\gamma}}_f + c_f \boldsymbol{\nabla}_0 \bar{\gamma}_f \cdot \boldsymbol{\nabla}_0 \dot{\bar{\gamma}}_f \rangle_{V_0} = 0 \,. \end{cases} \tag{47}$$

In the next Section, the boundary conditions are specified in order to satisfy *a priori* the Hill-Mandel principle.

3.2. Hill-Mandel principle and homogenized quantities

The Hill-Mandel condition, so-called the macro-homogeneity condition, allows considering mechanical constitutive relations through different scales in a consistent way [1]. The most common condition refers to the equality between the deformation power at a macroscopic point and the volume averaging deformation power over the whole SMVE, yielding

$$\left\langle \mathbf{P} : \dot{\mathbf{F}} \right\rangle_{V_0} = \bar{\mathbf{P}} : \dot{\bar{\mathbf{F}}} \,, \tag{48}$$

where $\bar{\mathbf{P}}$ is the macroscopic first Piola-Kirchhoff stress tensor and where $\bar{\mathbf{F}}$ is the macroscopic deformation gradient tensor. Using the integration by parts and the local equilibrium equation specified in Eq. (40), Eq. (48) can be rewritten as

$$\frac{1}{|V_0|} \int_{\partial V_0} \dot{\mathbf{u}} \cdot \mathbf{T} \, dA = \bar{\mathbf{P}} : \dot{\bar{\mathbf{F}}} \,. \tag{49}$$

Clearly, $\bar{\mathbf{P}} : \dot{\bar{\mathbf{F}}}$ is the external power which drives the deformation state of the microscopic boundary value problem. From Eq. (49), the weak form (47) is rewritten as

$$\begin{cases} \langle \mathbf{P} : (\dot{\mathbf{u}} \otimes \boldsymbol{\nabla}_0) \rangle_{V_0} - \bar{\mathbf{P}} : \dot{\bar{\mathbf{F}}} = 0 \,, \\ \langle (\bar{\gamma} - \gamma) \dot{\bar{\gamma}} + c_s \boldsymbol{\nabla}_0 \bar{\gamma} \cdot \boldsymbol{\nabla}_0 \dot{\bar{\gamma}} \rangle_{V_0} = 0 \,, \\ \langle (\bar{\gamma}_f - \gamma_f) \dot{\bar{\gamma}}_f + c_f \boldsymbol{\nabla}_0 \bar{\gamma}_f \cdot \boldsymbol{\nabla}_0 \dot{\bar{\gamma}}_f \rangle_{V_0} = 0 \,. \end{cases} \tag{50}$$

Once the Hill Mandel condition is satisfied following Eq. (49), the macroscopic quantities are estimated by volume averaging

$$\dot{\bar{\mathbf{F}}} = \left\langle \dot{\mathbf{F}} \right\rangle_{V_0} \,, \text{ and} \tag{51}$$

$$\bar{\mathbf{P}} = \langle \mathbf{P} \rangle_{V_0} \,. \tag{52}$$

Following an integration by parts and the Gauss' theorem application, these last two equations are rewritten

as

$$\dot{\bar{\mathbf{F}}} \quad = \quad \frac{1}{|V_0|} \int_{\partial V_0} \dot{\mathbf{u}} \otimes \mathbf{N} \, dA \,, \text{ and} \tag{53}$$

$$\bar{\mathbf{P}} \quad = \quad \frac{1}{|V_0|} \int_{\partial V_0} \mathbf{T} \otimes \mathbf{X} \, dA \,. \tag{54}$$

The microscopic boundary condition of the displacement field $\mathbf{u}$ is chosen in order to satisfy *a priori* the Hill-Mandel condition (49) and Eq. (53). The latter leads to the kinematically admissible space of the displacement field while Eq. (46) allows defining the ones of the nonlocal variables. When only the integral forms (46, 53) are considered to define the boundary conditions, the weakest kinematic constraints are obtained. In the context of the kinematically admissible finite elements, stronger conditions are generally used. The periodic boundary condition (PBC) is often used in combination with the assumption of the periodic distribution of fibers. Although the SMVE generated following [9] is generally not periodic, the periodic boundary condition is still favored as it improves the convergence rate [21]. Because the PBC results in a SMVE deformed shape compatible with the periodic assumption, multiple localization bands can appear in the post-peak localization stage, which is nonphysical since only one band develops [22]. This nonphysical result can be avoided using orthogonal uniform mixed boundary conditions [3], or the minimal kinematic boundary condition [23] in which the localization direction can freely develop, or the percolated path-aligned boundary condition [22] in which the boundary condition is adapted with the direction of the localization band. Under tensile loading conditions, experimental and numerical studies reveal that the failure band is perpendicular to the loading direction [7]. When only one localization band develops, the use of the periodic boundary condition is still valid. Under compressive loading, the failure pattern is oriented with an angle so that multiple failure bands occur [6], and the use of the periodic boundary condition after the onset of localization is not appropriate [22]. In this work, only PBC is considered: under tensile loading, the failure characteristics are extracted, while under compressive loading only the material strength is of interest for validation purpose.

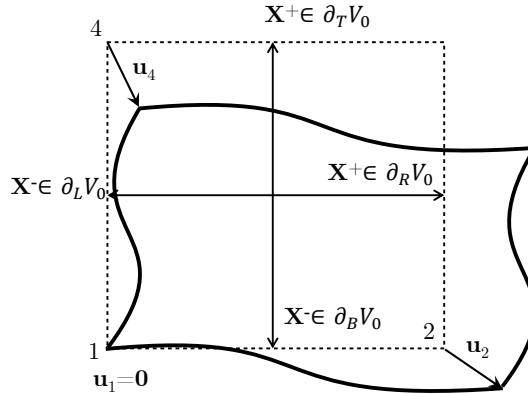### 3.3. Boundary condition for the displacement field

Figure 3: Periodic boundary conditions

The periodic boundary condition (PBC) of the displacement field $\mathbf{u}$ adds extra constraints to the ones defined by Eqs. (49, 53). The whole boundary ∂V_0 can be decomposed into negative and positive parts such that $\partial_- V_0 = \partial_L V_0 \cup \partial_B V_0$ and $\partial_+ V_0 = \partial_R V_0 \cup \partial_T V_0$. Each material point $\mathbf{X}^- \in \partial_- V_0$ matches with a material point $\mathbf{X}^+ \in \partial_+ V_0$ to form a couple of matching nodes $(\mathbf{X}^-, \mathbf{X}^+)$, see Fig. 3. The periodic boundary condition is then expressed by the periodicity of the displacement field and anti-periodicity of the traction

field on the matching nodes, such that

$$
\begin{cases}
\dot{\mathbf{u}}\left(\mathbf{X}^+\right) - \dot{\mathbf{u}}\left(\mathbf{X}^-\right) = \dot{\bar{\mathbf{F}}} \cdot \left(\mathbf{X}^+ - \mathbf{X}^-\right), \\
\mathbf{T}\left(\mathbf{X}^+\right) = -\mathbf{T}\left(\mathbf{X}^+\right),
\end{cases}
\tag{55}
$$

where $\bar{\mathbf{F}}$ is the homogenized deformation gradient given in Eq. (53). With the use of the PBC, the left hand side of the Hill Mandel condition (49) is rewritten as

$$
\frac{1}{|V_0|} \int_{\partial V_0} \mathbf{T} \cdot \dot{\mathbf{u}} \, dA = \int_{\partial_- V_0} \mathbf{T} \otimes \left(\mathbf{X}^+ - \mathbf{X}^-\right) dA : \dot{\bar{\mathbf{F}}} = \bar{\mathbf{P}} : \dot{\bar{\mathbf{F}}},
\tag{56}
$$

since the homogenized stress is estimated by Eq. (54). Therefore, one can conclude that the PBC satisfies the Hill-Mandel condition. For general non-periodic meshes, the point-to-point constraints expressed in Eq. (55) cannot directly be applied. This problem can be resolved with the interpolation method proposed by [21], in which an interpolation form is introduced to approximate the PBC, such as

$$
\begin{cases}
\dot{\mathbf{u}}\left(\mathbf{X}^-\right) & = \sum_{i=1}^N \mathbb{N}_i\left(\mathbf{X}^-\right) \dot{\mathbf{v}}^i, \\
\dot{\mathbf{u}}\left(\mathbf{X}^+\right) & = \sum_{i=1}^N \mathbb{N}_i\left(\mathbf{X}^-\right) \dot{\mathbf{v}}^i + \dot{\bar{\mathbf{F}}} \cdot \left(\mathbf{X}^+ - \mathbf{X}^-\right),
\end{cases}
\tag{57}
$$

where $\sum_{i=1}^N \mathbb{N}_i\left(\mathbf{X}^-\right) \dot{\mathbf{v}}^i$ is the interpolation form of degree N, which is defined from the discrete field $\dot{\mathbf{v}}^i$ and its shape functions $\mathbb{N}_i\left(\mathbf{X}^-\right)$, with $i = 1, \ldots, N$.

3.4. Boundary conditions for nonlocal variables

The boundary conditions related to the nonlocal variables are defined in order to satisfy *a priori* Eqs. (46). If no other constraints are considered, Eq. (46) leads to the following homogeneous Neumann-type boundary condition [19]

$$
\boldsymbol{\nabla}_0 \varphi \cdot \mathbf{N}^\Gamma = 0, \text{ on } \Gamma_0,
\tag{58}
$$

where φ is a nonlocal variable representing either $\bar{\gamma}$ or $\bar{\gamma}_f$, where $\Gamma_0 = \partial V_0 \cup \partial_I V_0$, and where $\mathbf{N}^\Gamma$ is the outward unit normal of Γ_0 in the reference configuration (either $\mathbf{N}$ of ∂V_0 or $\mathbf{N}^I$ of $\partial_I V_0$). Equation (58) implies an insulating condition, in which no direct nonlocal energy exchange exists with the surroundings of the body bounded by Γ_0: the net dissipation in this body vanishes for constant damage [20]. If the boundary of interest is the boundary of the SMVE, the influence of the surrounding is always present so that this insulating statement appears to be too ideal. When multiple materials are present (fiber and matrix in composites), the nonlocal energy exchange across the dissimilar interfaces needs to be considered. If the condition (58) is still used, the nonlocal energy exchange across the dissimilar interfaces is suppressed and the ability of the elastic region to influence damage growth in the process zone is limited, preventing length scale effects to be accounted for.

A complete discussion on the thermodynamics aspects of the boundary condition for nonlocal variables can be found in [20]. In this work, the boundary conditions of the nonlocal variables are derived from the weak conditions given in the system of Eqs. (46). Using the decomposition of the boundary ∂V_0 into negative and positive parts as sketched out in Fig. 3, the two first equations of the system of equations (46) can be rewritten as

$$
\left\{ \int_{\partial V_0^-} [\![c_s \boldsymbol{\nabla}_0 \bar{\gamma} \dot{\bar{\gamma}}]\!] \cdot \mathbf{N}^- dA = 0, \int_{\partial V_0^-} [\![c_f \boldsymbol{\nabla}_0 \bar{\gamma}_f \dot{\bar{\gamma}}_f]\!] \cdot \mathbf{N}^- dA = 0, \right.
\tag{59}
$$

where the definitions of the jump and mean operators expressed in Eqs. (45) are extended onto the external surface ∂V_0 by

$$
\begin{cases}
[\![\bullet]\!] = \bullet \left(\mathbf{X}^+\right) - \bullet \left(\mathbf{X}^-\right), \\
\langle \bullet \rangle = \frac{1}{2} \left[\bullet \left(\mathbf{X}^+\right) + \bullet \left(\mathbf{X}^-\right) \right],
\end{cases}
\tag{60}
$$

where $\mathbf{X}^+ \in \partial^+ V_0$ matches $\mathbf{X}^- \in \partial^- V_0$ to form a matching nodes pair.

Using the equality $[\![ab]\!] = [\![a]\!] \langle b \rangle + \langle a \rangle [\![b]\!]$ with two arbitrary quantities a and b, the system of equations (46) becomes

$$\int_{\Gamma_0} \left([\![c\boldsymbol{\nabla}_0\varphi]\!] \cdot \mathbf{N}^\Gamma \langle \dot{\varphi} \rangle + \langle c\boldsymbol{\nabla}_0\varphi \rangle \cdot \mathbf{N}^\Gamma [\![\dot{\varphi}]\!] \right) dA = 0, \tag{61}$$

where φ represents a nonlocal variable, and where c is the square of its nonlocal length. In order to satisfy *a priori* Eq. (61), Γ_0 is divided into different non-overlapping subsets such that $\Gamma_0 = \bigcup_i \Gamma_0^i$, and one of the three following possible kinds of boundary conditions is used for the nonlocal variable φ on each $\Gamma_0^i \subset \Gamma_0$

i) Fixation:

$$\dot{\varphi} = 0 \text{ on } \Gamma_0^i. \tag{62}$$

ii) Isolation:

$$\boldsymbol{\nabla}_0\varphi \cdot \mathbf{N}^\Gamma = 0, \text{ on } \Gamma_0^i. \tag{63}$$

iii) Balance:

$$\begin{cases} [\![c\boldsymbol{\nabla}_0\varphi]\!] \cdot \mathbf{N}^\Gamma = 0 \\ [\![\dot{\varphi}]\!] = 0 \end{cases} \text{ on } \Gamma_0^i. \tag{64}$$

One can find that the condition (62) is a full kinematic constraint, which is equivalent to the linear displacement boundary condition of the displacement field, Eq. (58) is equivalent to the constant traction boundary condition and Eq. (64) is equivalent to the periodic boundary condition of the displacement field. Note that the variational statement does not require to constrain directly the condition $[\![c\boldsymbol{\nabla}_0\varphi]\!] \cdot \mathbf{N}^\Gamma = 0$ in the last condition while kinematic constraints on the nonlocal variable $\dot{\varphi} = 0$ or $[\![\dot{\varphi}]\!] = 0$ must be directly enforced in the context of kinematically admissible finite element. Since the damage variables are defined as functions of the nonlocal variables, the condition (62) suppresses the damage band extending to the boundary of the domain. Therefore, the conditions (63) and (64) are considered in this work.

3.4.1. At the external boundary ∂V_0

At the external boundary ∂V_0, the boundary condition for nonlocal variables should be compatible with the ones of the displacement field. Since the PBC is used for the displacement field, the balance condition (64) is used for both $\bar{\gamma}$ and $\bar{\gamma}_f$.

The implementation of the point-to-point constraints $[\![\dot{\varphi}]\!] = 0$ requires periodic meshes. As the mesh is not periodic in general, the interpolation method [21] is used as with the periodic boundary condition of the displacement field expressed in Eq. (57), leading to

$$\dot{\varphi}\left(\mathbf{X}^-\right) = \dot{\varphi}\left(\mathbf{X}^+\right) = \sum_{i=1}^{M^\varphi} \mathbb{M}_i^\varphi\left(\mathbf{X}^-\right) \dot{\varphi}^i, \tag{65}$$

where φ represents either $\bar{\gamma}$ or $\bar{\gamma}_f$, and where $\sum_{i=1}^{M^\varphi} \mathbb{M}_i^\varphi\left(\mathbf{X}^-\right) \varphi^i$ is the interpolation form of degree M^φ, which is defined from the discrete field φ^i and its shape functions $\mathbb{M}_i^\varphi\left(\mathbf{X}^-\right)$, with $i = 1, \ldots, M^\varphi$. In all generalities, the interpolation forms of the nonlocal variables and the one of the displacement field are independent. In this work, the same forms are used, so that $N = M^{\bar{\gamma}} = M^{\bar{\gamma}_f}$ and $\mathbb{N}_i\left(\mathbf{X}^-\right) = \mathbb{M}_i^{\bar{\gamma}}\left(\mathbf{X}^-\right) = \mathbb{M}_i^{\bar{\gamma}_f}\left(\mathbf{X}^-\right)$, with $i = 1, \ldots, N$.

3.4.2. At the internal boundary $\partial_I V_0$

For the nonlocal plastic strain field $\bar{\gamma}$, either the isolation condition (63) or the balance condition (64) can be used *a priori* at the internal boundary $\partial_I V_0$. However, we will show in the next section, that only

the balance condition can be used to introduce a length scale effect resulting from the presence of fibers within the matrix.

For the nonlocal failure plastic strain field $\bar{\gamma}_f$, since the failure occurs at the interphase region close to the fiber, the isolation condition (63) should be used.

3.5. Finite element resolution

Unlike the FE² scheme in which the microscopic boundary value problem is directly driven by the macroscopic deformation gradient available at every macroscopic material point, a virtual test is performed under a prescribed deformation mode. Several components of the homogenized deformation gradient tensor as well as of the homogenized stress tensor are unknown. Therefore a specific strategy is proposed to obtain the prescribed deformation mode:

- Control nodes are defined on which prescribed displacements or prescribed forces are applied in order to obtain the prescribed deformation mode; they are denoted by 1, 2, and 4, see Fig. 2.

- The microscopic boundary conditions described in Section 3.3 and Section 3.4 are used and specified by relating the degrees of freedom of other nodes to the ones of the control nodes, *i.e.* nodes 1, 2, and 4 shown in Fig. 2.

- The finite element discretization of the weak form (50) combined to the micro-scale boundary conditions listed here above results in a system of multi-point constraints, which can be treated through the unified scheme developed in [24].

When snapback occurs, a path following technique must be used to follow the whole fracture process. In this case, the procedure described above is mandatory since prescribed forces must be used instead of prescribed displacements. Besides, the response of a structure made of dissipative solids generally follows an irreversible equilibrium path, which is characterized by an increase of the dissipated energy. The total dissipated energy, denoted by Υ_{V_0}, can be estimated by

$$\Upsilon_{V_0}(t) = \int_{V_0} \int_0^t \dot{\Upsilon}_m \, dt \, dV \,, \tag{66}$$

where $\dot{\Upsilon}_m$ is locally estimated by Eq. (39). As a result, by constraining the amount of the dissipated energy Υ_{V_0} at each increment step, the equilibrium path can be automatically traced [15]. This virtual testing strategy using the path following technique based on dissipated energy is detailed in Appendix A.

3.6. Extraction of the homogenized properties

The homogenized behavior, *i.e.* the homogenized stress evolution (52) in terms of the homogenized deformation gradient (51), is obtained by volume averaging. As a result, the macroscopic Cauchy stress is computed by

$$\bar{\boldsymbol{\sigma}} = \frac{1}{\bar{J}} \bar{\mathbf{P}} \cdot \bar{\mathbf{F}}^T \,, \tag{67}$$

where $\bar{J} = \det \bar{\mathbf{F}}$ is the macroscopic Jacobian. During the softening stage, the homogenized response in terms of stress and strain measures depends on the dimensions of the microscopic problems. However, the objectivity can be recovered by considering the homogenized TSL [2, 3]. The homogenized TSL can be directly estimated on-the-fly for concurrent multiscale simulations [25]. However, this work focuses on non-concurrent simulations and on the extraction, from the resolution of the microscopic problems, of the cohesive strength, denoted by $\bar{\sigma}_c$, which characterizes the onset of the creak nucleation, and the critical energy release rate, denoted by $\bar{G}_c$, which characterizes the total fracture energy released per unit crack surface opening. The extraction of these two parameters is detailed in the following.

After the onset of microscopic localization, a macroscopically homogeneous state cannot be considered over the SMVE, but a homogenized elastic state can be enriched by a cohesive band Γ_0, whose unit normal
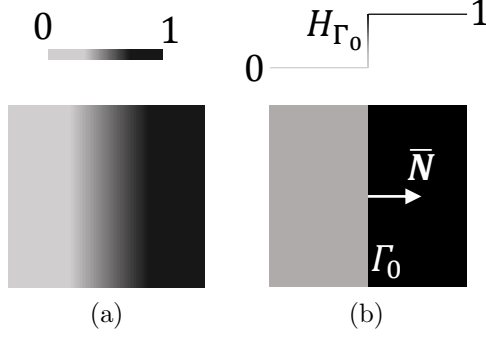
16

Figure 4: Enrichment of the position field: (a) position distribution of the microscopic problem after the onset of localization, (b) equivalent inhomogeneous homogenized state with an embedded cohesive layer Γ_0 whose unit normal vector is $\bar{\mathbf{N}}$. The discontinuous position field is enriched by a cohesive jump using the Heaviside function H_{Γ_0}.

vector is $\bar{\mathbf{N}}$, at the location of the microscopic localization band, see Fig. 4. Although the microscopic position field does not exhibit sharp discontinuity, the macroscopic one is enhanced with a cohesive discontinuity as

$$\dot{\bar{\mathbf{x}}} = \dot{\bar{\mathbf{x}}}^c + H_{\Gamma_0}\dot{\bar{\mathbf{\Delta}}}\,, \tag{68}$$

where $\bar{\mathbf{x}}$ is the macroscopic position vector, $\bar{\mathbf{x}}^c$ is its continuous counterpart, H_{Γ_0} is a Heaviside function over Γ_0, which is a discontinuous step function, and where $\bar{\mathbf{\Delta}}$ is the homogenized cohesive jump. The macroscopic deformation gradient is then estimated using the volume averaging principle (51)

$$
\begin{aligned}
\dot{\bar{\mathbf{F}}} &= \left\langle \left(\dot{\bar{\mathbf{x}}}^c + H_{\Gamma_0}\dot{\bar{\mathbf{\Delta}}}\right) \otimes \boldsymbol{\nabla}_0 \right\rangle_{V_0} \\
&= \left\langle \dot{\bar{\mathbf{x}}}^c \otimes \boldsymbol{\nabla}_0 + \delta_{\Gamma_0}\dot{\bar{\mathbf{\Delta}}} \otimes \bar{\mathbf{N}} \right\rangle_{V_0} \\
&= \dot{\bar{\mathbf{F}}}^c + \frac{A_0}{V_0}\dot{\bar{\mathbf{\Delta}}} \otimes \bar{\mathbf{N}}\,,
\end{aligned}
\tag{69}
$$

where $\dot{\bar{\mathbf{F}}}^c$ is the macroscopic continuous deformation gradient, $H_{\Gamma_0} \otimes \boldsymbol{\nabla}_0 = \delta_{\Gamma_0}\bar{\mathbf{N}}$ is defined using the Dirac function δ_{Γ_0}, and where

$$A_0 = \int_{V_0} \delta_{\Gamma_0}\, dV\,. \tag{70}$$

From the last equation, A_0 represents the homogenized crack size embedded in the SMVE.

By applying the Hill-Mandel principle (48) using the macroscopic deformation gradient given in Eq. (69), one has

$$V_0\left\langle \mathbf{P} : \dot{\mathbf{F}} \right\rangle_{V_0} = V_0\bar{\mathbf{P}} : \dot{\bar{\mathbf{F}}}^c + A_0\bar{\mathbf{T}} : \dot{\bar{\mathbf{\Delta}}}\,, \tag{71}$$

where the cohesive traction $\bar{\mathbf{T}}$ is given by

$$\bar{\mathbf{T}} = \bar{\mathbf{P}} \cdot \bar{\mathbf{N}}\,. \tag{72}$$

Equation (71) can be integrated from the onset of microscopic localization occurring at time t^{loc} until final

17

failure, leading to

$$V_0 \int_{t^{\mathrm{loc}}}^{+\infty} \left\langle \mathbf{P} : \dot{\mathbf{F}} \right\rangle_{V_0} dt = V_0 \int_{t^{\mathrm{loc}}}^{+\infty} \bar{\mathbf{P}} : \dot{\bar{\mathbf{F}}}^c dt + A_0 \int_{t^{\mathrm{loc}}}^{+\infty} \bar{\mathbf{T}} \cdot \dot{\bar{\boldsymbol{\Delta}}} dt \,. \tag{73}$$

Since an elastic contribution is released through an elastic unloading state over the continuous part $\bar{\mathbf{F}}^c$ of the SMVE, one has

$$V_0 \int_{t^{\mathrm{loc}}}^{+\infty} \left\langle \mathbf{P} : \dot{\mathbf{F}} \right\rangle_{V_0} dt - V_0 \int_{t^{\mathrm{loc}}}^{+\infty} \bar{\mathbf{P}} : \dot{\bar{\mathbf{F}}}^c dt = \Upsilon_{V_0}^{\mathrm{end}} - \Upsilon_{V_0}^{\mathrm{loc}} \,, \tag{74}$$

where $\Upsilon_{V_0}^{\mathrm{loc}}$ and $\Upsilon_{V_0}^{\mathrm{end}}$ are respectively the accumulated microscopic dissipation values over the SMVE at the onset of microscopic localization and at the final failure states. These quantities are estimated using Eq. (66). Moreover, the critical energy release rate is estimated by

$$\bar{G}_c = \int_{t^{\mathrm{loc}}}^{+\infty} \bar{\mathbf{T}} \cdot \dot{\bar{\boldsymbol{\Delta}}} dt \,. \tag{75}$$

As a result, the critical energy release rate can be extracted from the microscopic accumulated dissipation by the following equation

$$\bar{G}_c = \frac{\Upsilon_{V_0}^{\mathrm{end}} - \Upsilon_{V_0}^{\mathrm{loc}}}{A_0} \,. \tag{76}$$

The cohesive tension magnitude, denoted by $\bar{\sigma}$, is defined in the current configuration as

$$\bar{\sigma} = \| \bar{\boldsymbol{\sigma}} \cdot \bar{\mathbf{n}} \| \,, \tag{77}$$

where $\| \bullet \| = \sqrt{\bullet \cdot \bullet}$ is the vector norm, and $\bar{\mathbf{n}}$ is the unit normal vector of the localization band in the current configuration, which can be estimated from its reference counterpart and the macroscopic deformation gradient at the onset of microscopic localization using Nanson's relation as

$$\bar{\mathbf{n}} = \frac{\bar{\mathbf{F}}^{-T} \cdot \bar{\mathbf{N}}}{\| \bar{\mathbf{F}}^{-T} \cdot \bar{\mathbf{N}} \|} \tag{78}$$

The cohesive strength σ_c is then defined by the maximal value of the cohesive traction magnitude, such as

$$\bar{\sigma}_c = \max \left[\sigma \left(\tau \right) ; \tau \in \left[0 \, \infty \right) \right] \,. \tag{79}$$
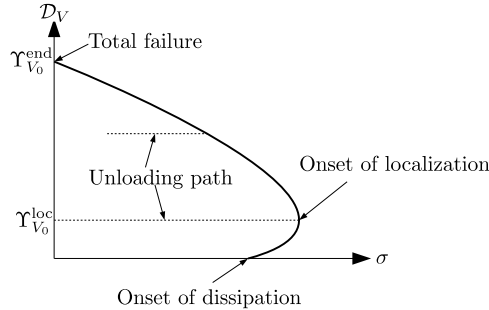
Figure 5: Failure diagram representing the dissipated energy as a function of the magnitude of the cohesive traction.

18

Both the cohesive strength $\bar{\sigma}_c$ and the critical energy release rate $\bar{G}_c$ can be deduced from the failure diagram of the evolution of the total dissipated energy with respect to the magnitude of the cohesive traction, as shown in Fig. 5. Under macroscopic loading condition, the accumulated dissipated energy and the magnitude of the cohesive traction are evaluated from Eq. (66) and Eq. (77). The cohesive traction in the current configuration is considered in order to detect the onset of strain softening while the total dissipated energy is estimated in the reference configuration since the constitutive formulation follows the total Lagrange formalism. From this diagram, three distinct stages are observed

- The linear elastic stage is characterized by a zero dissipated energy.

- The prepeak nonlinear stage starts from the onset of the dissipation until reaching the peak cohesive traction. In this stage, the damage of material constituents diffuses in the whole microstructure. This part of the dissipated energy scales with the volume of the microstructure.

- The post-peak localization stage is characterized by a decrease of the cohesive traction from its peak to zero, which corresponds to the total failure at the microscopic scale. Clearly, this stage definition is based on the assumption that the crack nucleation occurs at the peak value of the cohesive traction. Since the localization starts developing at the microscopic scale, the dissipated energy released during this stage does not scale with the volume of the microstructure. At the same time, the macroscopic crack nucleates and develops. From the balance of the dissipated energy, the total energy dissipated at the macroscopic scale by the homogenized TSL should be equal to the total dissipated energy released during this stage.

From the failure diagram, the dissipated energy cannot decrease as a result of the second law of thermodynamics. An elastic unloading step corresponds to a constant dissipated energy. Finally, the two relevant parameters of the homogenized cohesive law are estimated using Eqs. (76, 79).

4. Material constituents parameters identification and experimental validation

In this section, the behavior of carbon fibers reinforced high-crosslinked epoxy matrix is studied using the micromechanics model developed in Section 3. The matrix is the RTM6 epoxy resin that has been experimentaly tested in [10]. Unidirectional composites slabs with carbon fibers were manufactured by RTM in order to perfectly replicate the curing conditions of the bulk matrix. An analysis of micrography obtained with an optical microscope at randomly chosen spots in the slab enabled the calculation of an average fiber volume fraction of around 40%. The details about fabrication and testing procedures can be found in [8]. The testing results are used in this work for identification and validation purposes. The SMVEs are first defined from the geometrical measurements. Since the constitutive model of the matrix relies on the phenomenological consideration, its parameters are then identified based on experimental stress-strain curves. Because of the length scales incorporated in the constitutive law, a unique set of material parameters can be found to capture the experimental stress-strain curves of pure resin and composites.

4.1. Definition of the SMVEs

In order to perform the numerical simulations with a realistic microstructure of fiber reinforce composites, the fiber distribution and the fiber diameters must be close to the ones of the real microstructure. For this purpose, the composite microstructure is generated from the statistical characterizations estimated from SEM images of a similar material system [9] but limiting the average volume fraction of fibers to 40%. The generating procedure in [9] can be summarized as follows:

(i) extract the statistical characterizations of the microstructure from SEM images of a similar material system;

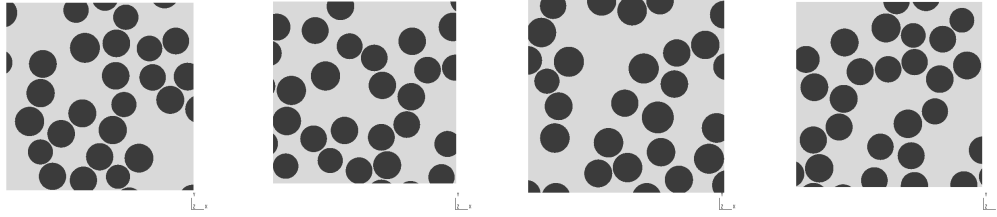(ii) construct a micro-informatics model able to generate microstructure satisfying the same statistical indicators;

19

Figure 6: Some SMVEs of dimensions of 40 μm×40 μm.

(iii) generate a large microstructure using this micro-informatics model;

(iii) extract SMVEs by moving a window of given sizes throughout this large microstructure; as a result of the existing randomness, the volume fraction of fibers in each SMVE is not equal to 40%;

Fig. 6 shows 4 SMVEs with a moving window of dimensions 40 μm×40μm. Clearly, with this methodology there is no periodicity of fiber distribution on the opposite edges of an SMVE as it is a part of a real microstructure, for which such a periodicity is not observed. Adding a periodicity constraint on the boundary for SMVEs of reduced sizes would actually modify the microstructure statistical characteristics. However the periodic boundary condition can still be enforced with the use of the interpolation method proposed in [21].

4.2. Identification of model parameters

Table 1: Material parameters of the carbon fibers from [3]

Longitudinal Young's modulus	E_L	230	[GPa]
Transverse Young's modulus	E_T	40	[GPa]
Transverse Poisson's ratio	ν_TT	0.20	[-]
Longitudinal-Transverse Poisson's ration	ν_LT	0.256	[-]
Transverse shear modulus	G_TT	16.7	[GPa]
Longitudinal-Transverse shear modulus	G_LT	24	[GPa]

The carbon fibers are assumed to be linear elastic and transversely isotropic as presented in Section 2.1. Their material constants are reported in Tab. 1. The RTM6 epoxy matrix follows a viscoelastic-viscoplastic-damage model as discussed in Section 2.2. Following [12], its model parameters are calibrated against the experimental results in the cases of the pure RTM6 epoxy resin subjected to uniaxial tensile and compressive loading conditions. However, this set of material parameters is not unique. As demonstrated in Fig. 7, without considering the failure stage, the same stress-strain curves can be obtained by simultaneously modifying the hardening moduli given by Eqs. (21) and the saturation softening law given by Eq. (22). Clearly, each set of parameters is characterized by a given value of $D_{s\infty}$. The identification procedure performed in [12] cannot be used to predict $D_{s\infty}$ since this parameter does not affect the global result when only uniform and uniaxial tensile and compressive tests are used. It motivates using other tests in which the nonlocal softening variable D_s exhibits localization. In this work, the identification considers the uniaxial compression tests of composites performed in [8] in combination with the experimental tests of the pure RTM6 epoxy resin performed in [12].

4.2.1. Pre-failure parameters of the RTM6 resin

In this section, only the parameters related to the softening law are identified: the other model parameters identified in [12] are reported in Tabs. 2 and 3. Therefore, while the parameters listed in Tabs. 2 and 3
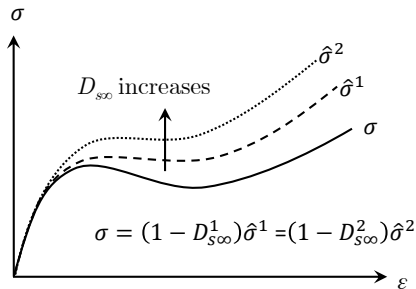
20

Figure 7: Different saturation softening models leading to the same stress-strain curve.

Table 2: Viscoelastic material parameters of the RTM6 epoxy resin from [12]

Number of Maxwell elements: 4 $E_\infty = 2450$ [MPa] $\nu = 0.39$ [-]	$E_1 = 380$	[MPa]	$g_1 = k_1 = 7000$	s
	$E_2 = 190$	[MPa]	$g_2 = k_2 = 70$	s
	$E_3 = 95$	[MPa]	$g_3 = k_3 = 0.7$	s
	$E_4 = 48$	[MPa]	$g_4 = k_4 = 0.07$	s

remain unchanged, the expressions of the saturation softening law and of hardening moduli previously identified in [12], and reported in Tab. 4 for indication purpose, are modified.

The experimental results of the pure RTM6 resin tests conducted in [12] are first considered. The stress-strain curve under uniaxial compression at a constant engineering strain rate of $-1.4\,10^{-3}$ s^{-1} is used as the reference curve. The same calibration procedure used in [12] is reconsidered with other values of $D_{s\infty}$: 0.31, 0.51, and 0.62. The new saturation softening laws and new hardening moduli are reported in Tab. 5. The stress-strain curves using these parameters under compressive and tensile loading conditions are shown in Figs. 8a and b, respectively. The nonlocal length scale of the nonlocal softening variable does not affect the global result since the deformation state is uniform.

The saturation softening law governs the evolution of the softening damage D_s whose value is limited by the saturation value $D_{s\infty} < 1$. In this case, the material never loses its entire load bearing capability. Once D_s is saturated by its limit value, the loss of ellipticity no longer occurs and the local formulation should follow [26]. This decreasing nonlocal effect can be obtained by decreasing the nonlocal length scale when D_s develops [26]. For this purpose, the nonlocal length scale is defined as a function of the softening variable itself

$$c_s = l^2(1 - \frac{D_s}{D_{s\infty}}), \tag{80}$$

where l is the initial nonlocal length scale of the softening variable. Clearly, when $D_s = D_{s\infty}$, c_s vanishes and the local formulation is recovered. In order to directly integrate the effect of fibers, a fixed value $l = 3$ μm, which is the average radius of fiber [9], is considered in this work.

When considering the nonlocal interaction of the softening variable, the boundary condition of the non-local plastic strain at interfaces of fibers and matrix must be correctly chosen between the two possibilities described in Section 3.4: balance and isolation conditions. The influence of these kinds of boundary conditions is analyzed through a numerical test. The first SMVE of dimension 40 μm×40 μm in Fig. 6 is

Table 3: Viscoplastic material parameters of the RTM6 epoxy resin from [12]

Yield exponent	α	3.5	[-]
Initial plastic Poisson's ratio	ν_p	0.3	[-]
Rate sensitivity exponent	p	0.21	[-]
Viscosity parameter	η	$3\,10^4$	[MPa·s]

Table 4: Parameters of saturation softening and of hardening moduli of the RTM6 epoxy resin from [12]

Data identification	Properties	Unit
$D_{s\infty} = 0.2$	$D_s = 0.2\left[1 - \exp\left(-45\gamma^2\right)\right]$	[-]
	$\sigma_c^0 = 48$	[MPa]
	$\sigma_t^0 = 38.4$	[MPa]
	$H_c = 4180\exp\left(-76\gamma\right)$	[MPa]
	$H_t = 3344\exp\left(-76\gamma\right)$	[MPa]
	$H_b = 340\gamma - 1320\gamma^2 + 4400\gamma^3$	[MPa]

Table 5: New parameters of saturation softening and of hardening moduli of the RTM6 epoxy resin

Data identification	Properties	Unit
$D_{s\infty} = 0.31$	$D_s = 0.31\left[1 - \exp\left(-11\gamma\right)\right]$	[-]
	$\sigma_c^0 = 48$	[MPa]
	$\sigma_t^0 = 40.8$	[MPa]
	$H_c = 3932.5\exp\left(-55\gamma\right)$	[MPa]
	$H_t = 3342.6\exp\left(-55\gamma\right)$	[MPa]
	$H_b = 428.5\gamma - 1663.5\gamma^2 + 5545\gamma^3$	[MPa]
$D_{s\infty} = 0.51$	$D_s = 0.51\left[1 - \exp\left(-21\gamma\right)\right]$	[-]
	$\sigma_c^0 = 48$	[MPa]
	$\sigma_t^0 = 40.8$	[MPa]
	$H_c = 5267.5\exp\left(-43\gamma\right)$	[MPa]
	$H_t = 4477.4\exp\left(-43\gamma\right)$	[MPa]
	$H_b = 849.6\gamma - 3298.6\gamma^2 + 10995\gamma^3$	[MPa]
$D_{s\infty} = 0.62$	$D_s = 0.62\left[1 - \exp\left(-30\gamma\right)\right]$	[-]
	$\sigma_c^0 = 48$	[MPa]
	$\sigma_t^0 = 40.8$	[MPa]
	$H_c = 6475\exp\left(-37\gamma\right)$	[MPa]
	$H_t = 5503.8\exp\left(-37\gamma\right)$	[MPa]
	$H_b = 1412.7\gamma - 5484.8\gamma^2 + 18283\gamma^3$	[MPa]

loaded by a uniaxial compression at a true strain rate of $-10^{-2}\,\mathrm{s}^{-1}$. The numerical results are shown in Figs. 9a and b, for respectively the balance and isolation conditions. The experimental results provided in [8] for compressive loading of carbon fibers reinforced RTM6 matrix are also reported. On the one hand, Fig. 9b shows the numerical results using the isolation condition. Clearly the stress-strain responses are not sensitive to the saturation softening and quite far from the experimental one. As a result, the isolation boundary condition for the nonlocal plastic strain should not be used. On the other hand, the numerical results using the balance condition are sensitive to the saturation softening. The higher the value of $D_{s\infty}$ is, the higher the peak stress is obtained. By the fact that the objective of this work is to find a set of material parameters that allows capturing not only the behavior of pure RTM6 matrix but also its behavior within composites, the balance condition is a better choice compared to the isolation one. Note that in the current constitutive model, the compressive peak stress is mainly due to the presence of the softening variable while failure variable develops later after satisfying the condition of the failure onset expressed in Eq. (25).

Since the microstructure variability is an important factor that affects the homogenized prediction, a set of 10 SMVE realizations of dimension 40 μm×40 μm is considered, and the values of $D_{s\infty}$ ranges from 0.2 to 0.62 for each realization. The experimental results in [8] obtained at a true compressive loading of strain rate $-10^{-2}\,\mathrm{s}^{-1}$ are considered as reference. The comparison between numerical and experimental results is shown in Fig. 10, and confirms that $D_{s\infty} = 0.62$ is an accurate value. The set of parameters characterized by $D_{s\infty} = 0.62$ is chosen for the following analyses as it provides predictions in a good agreement with experimental results performed on pure RTM6 resin and on composite materials.
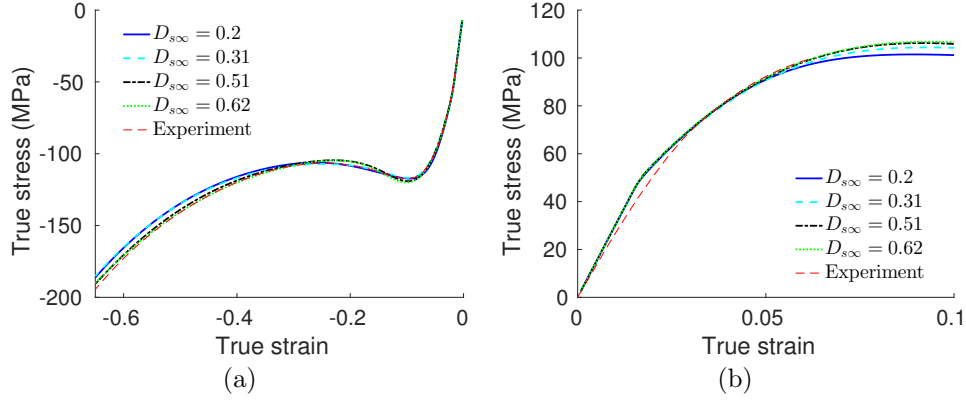
Figure 8: Model predictions with material data reported in Tab. 5 compared to the experimental results for compressive stress-strain response of the RTM6 epoxy resin: (a) under uniaxial compression at a constant engineering strain rate of $-1.4\,10^{-3}$ s^{-1} and (b) under uniaxial tension at a constant engineering strain rate of $-1.1\,10^{-3}$ s^{-1}.

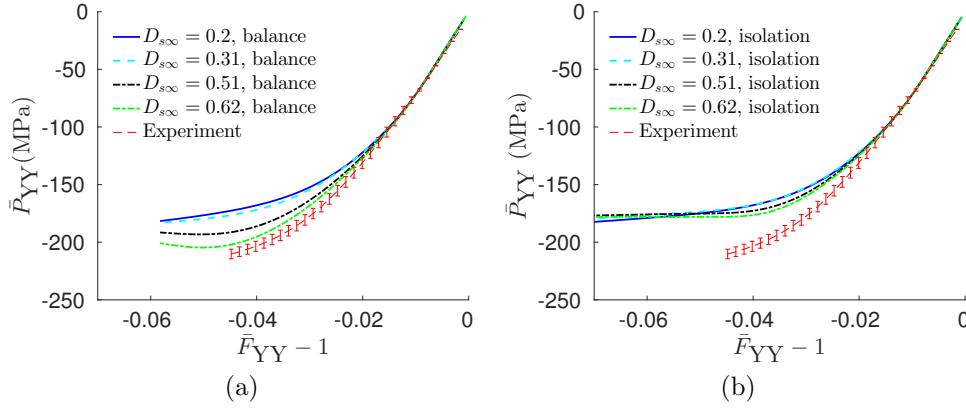Figure 9: Influence of boundary condition of the saturation nonlocal variable $\bar{\gamma}$ on interfaces between the fibers and the RTM6 matrix at a true strain rate of -10^{-2} s^{-1}: (a) balance condition and (b) isolation condition. Experimental results conducted on fiber reinforced RTM6 matrix from [8] are also reported.

4.2.2. Post-failure parameters of the RTM6 resin

Once the material parameters governing the behavior prior to the onset of failure are obtained, the ones governing the failure phase must be identified. The onset of failure is detected using Eq. (25) whose parameters were provided in [10]. However, since the current material formulation is not the same as the one considered in [10], the constants are modified by a factor f such that Eq. (25) can be rewritten as

$$\Phi_f = \gamma - f\left[a_0 \exp\left(-b_0 T\right) - c_0\right] = 0\,, \tag{81}$$

where $a_0 = 0.04042$, $b_0 = 7.815$, and $c_0 = 0.02558$ [10]. Since the material strength under uniaxial compressive loading at a constant engineering strain rate of $-1.4\,10^{-3}$ s^{-1} is approximately equal to 210 MPa [12], the coefficients of the failure surface (25) are given by

$$a = 0.03428\,, b = 7.815\,, \text{ and } c = 0.02169\,. \tag{82}$$

The nonlocal action of the failure variable is in all generality independent to the one of the softening variable. In this work however, their nonlocal length scales are assumed to be the same in order to ease of

23
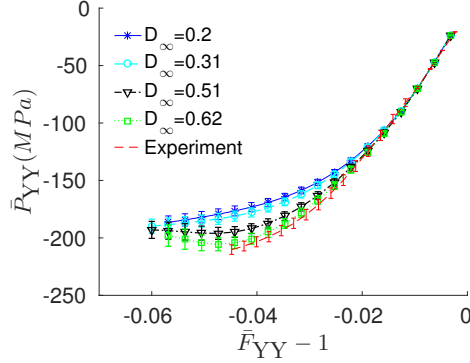
Figure 10: Influence of $D_{s\infty}$ on compressive responses of fiber reinforced RTM6 matrix at a true strain rate of $-10^{-2}\,\mathrm{s}^{-1}$.

the identification process, leading to

$$c_s = l^2(1 - \frac{D_s}{D_{s\infty}})\,,\text{and} \tag{83}$$

$$c_f = l^2\,. \tag{84}$$

Moreover, the critical energy release rate during the failure process under a specific loading condition, so-called G_c, is directly related to the nonlocal length scale and the failure law specified by Eq. (28). This failure law is characterized by three parameters: ζ_f, ζ_d, and χ_{fc}. By using $\zeta_f = 1$ and $\zeta_d = 0.3$ as considered in [12], the failure law is then controlled by χ_{fc} only, see Fig. 11a, where it can be seen that increasing χ_{fc} decreases the damage rate, leading to a more ductile behavior. The value of $G_c \approx 86.5\ \mathrm{J\cdot m^{-2}}$ was found for the pure RTM6 resin through experimental tests [27]. Moreover, the value of $l = 3\ \mathrm{\mu m}$ is fixed as described in the previous section. As a result, as G_c and l are known, the parameter χ_{fc} can be deduced by performing a virtual failure test as explained here below.
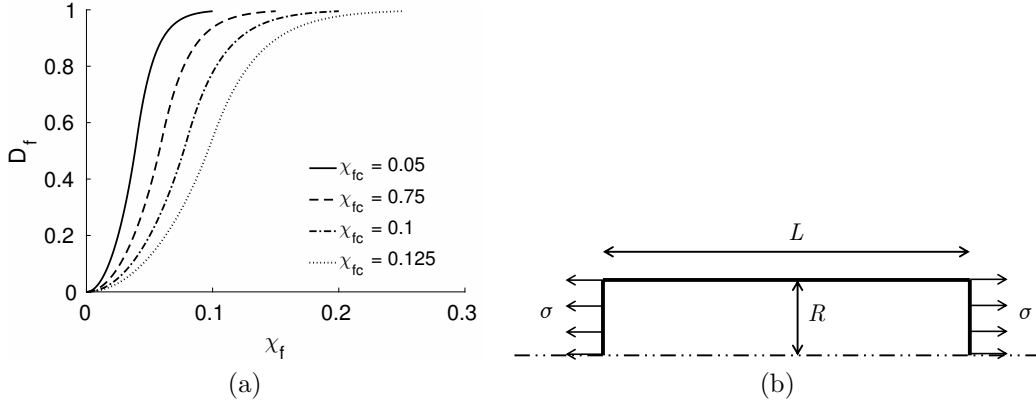
Figure 11: (a) Influence of χ_{fc} on the failure law and (b) cylindrical specimen of radius R and of length L considered in order to determe the critical energy release rate under uniaxial loading.

A virtual test using an axisymmetrical finite element formulation under a uniaxial loading condition is performed over a cylindrical specimen made of the pure RTM6 epoxy matrix, see Fig. 11b. The virtual specimen is defined by a length of L_0 and a radius of R_0. Since the finite element resolution converges when decreasing the mesh size as a result of using an implicit nonlocal formulation [19], a mesh sensitivity analysis was first performed to define the mesh for the subsequent analyzes. A very small reduction of the bar radius at the center is introduced to trigger localization deformation without affecting prelocalization stress-strain

24

curves. The elastic and plastic viscosity effects are not considered since the path following method based on the increase of the dissipated energy described in Section 3.5 is used because of the presence of the snapback for values of L_0 larger than l. From the total dissipation estimated by Eq. (66), the energy release rate G_c can be computed using Eq. (76). Because $A_0 = \pi R_0^2$, one has

$$G_c = \frac{\Upsilon_{V_0}^{\mathrm{end}} - \Upsilon_{V_0}^{\mathrm{loc}}}{\pi R_0^2} \ . \tag{85}$$

The true stress across the cylinder is estimated by

$$\sigma = \frac{F}{\pi R^2} \ , \tag{86}$$

where F is the longitudinal reaction force and where R is the current (in the deformed configuration) smallest cross-section radius. The value of $\Upsilon_{V_0}^{\mathrm{loc}}$ is measured when σ reaches its maximal value, which is by definition σ_c.
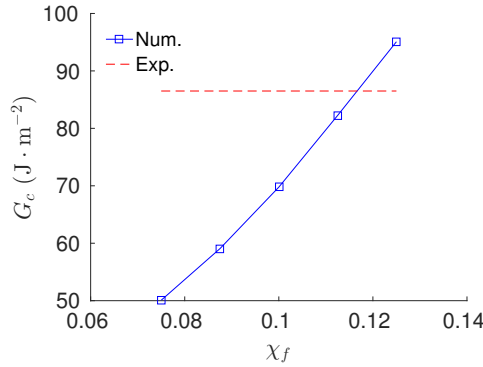
Figure 12: Influence of χ_{fc} with $l = 3 \ \mu\mathrm{m}$, $L_0 = 10l$, and $R_0 = 0.2l$.

From Eq. (85), clearly G_c is a function of L_0, R_0, l, and χ_{fc}. With the use of a dimensionless analysis, see Appendix B for details, one can introduce the dimensionless critical energy release rate that is a function of χ_{fc} only when the values of L_0 and R_0 are respectively large enough and small enough in comparison with the value of l. The evolution of G_c, which depends on χ_{fc} only (and of course on the material parameters), and not on the geometrical parameters, is depicted in Fig. 12 for $l = 3 \ \mu\mathrm{m}$, $L_0 = 10l$, and $R_0 = 0.2l$. From the value of $G_c \approx 86.5 \ \mathrm{J} \cdot \mathrm{m}^{-2}$ of the pure RTM6 resin [27], the value of $\chi_{fc} = 0.117$ is found.

4.3. Validation

In the previous section, the set of material parameters of the RTM6 epoxy resin was identified from experimental measurements of the pure matrix at a constant engineering strain rate of $-1.4 \, 10^{-3} \, \mathrm{s}^{-1}$ and of the composite at a constant true strain rate of $-10^{-2} \, \mathrm{s}^{-1}$. This set of material constants is used in this section to predict, not only the mechanical behavior of the pure RTM6 resin, but also the one of the composites at other strain rates. It will be shown that the predictions are in good agreement with experimental measurements.

4.3.1. Pure matrix

Figures 13 and 14 depict the comparison between the numerical predictions and the experimental results of the pure RTM6 epoxy resin under various constant engineering strain rates under uniaxial compression and uniaxial tension respectively. Under both uniaxial compressive and tensile loading conditions, a good agreement is obtained. Compared to the numerical prediction in [12], in which a rate independent failure surface is used, the new failure surface expressed by Eq. (25) allows modeling the effect of the strain rate on the onset of failure.
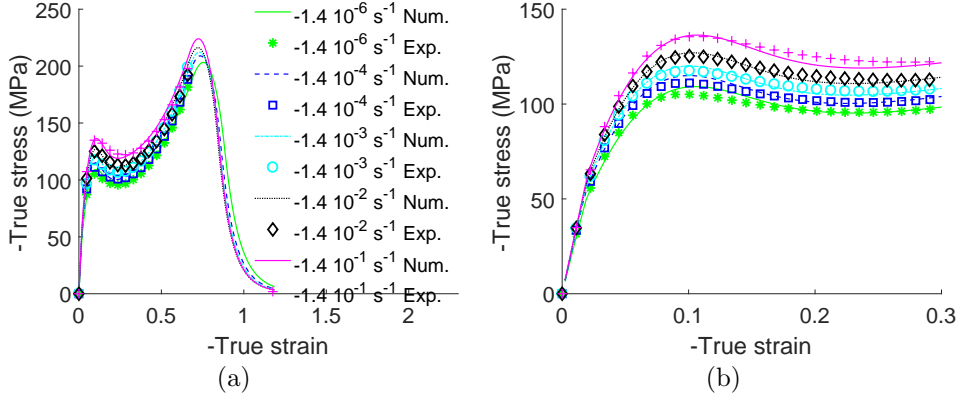
25

Figure 13: Model predictions compared to the experimental results of pure RTM6 epoxy resin under uniaxial compression: (a) full range and (b) zoom at small strains. Experimental results from [12] are also reported.
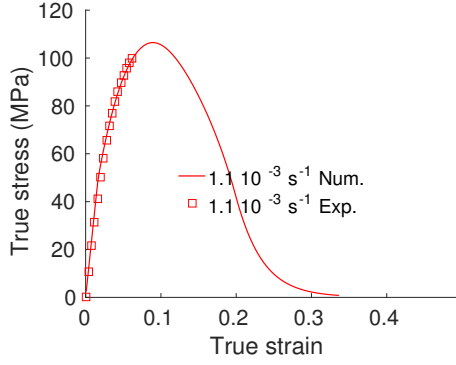

Figure 14: Model predictions compared to the experimental results of pure RTM6 epoxy resin under uniaxial tension. Experimental results from [12] are also reported.

4.3.2. Composite material

In case of composites, the 10 SMVEs used in Section 4.2.1 are reconsidered but this time by incorporating the failure model. Fig. (15) shows the numerical predictions in comparison with the experimental results obtained at constant true strain rates of -10^{-2} s^{-1}, -10^{-3} s^{-1}, and -10^{-4} s^{-1}. They display a good agreement for all three values of strain rates. Since the experimental specimens exhibit sudden failure, the experimental stress-strain curves do not exhibit the softening parts contrarily ot the numerical predictions.

Figure 16 shows the evolution of the distribution of the total damage variable D for the SMVE realization illustrated in Fig. 6a. The damage localizes in the matrix under the shape of shear bands, which are inclined to the loading direction in accordance with the literature, see *e.g.* [7]. Multiple localization bands appear as a result of using the PBC.

5. Application: extraction of the composite material failure characteristics

Once the material parameters of the fibers and of the RTM6 epoxy resin are identified, the homogenized cohesive properties, see Eqs. (79, 76), are extracted from the post-softening behavior.

To this end, and in order to study the size objectivity, a sequence of SMVEs of increasing dimensions is created, namely 20 μm×20 μm, 20 μm×40 μm, 20 μm×60 μm, and 20 μm×80 μm SMVEs are successively considered. For each size, several realizations are generated using the method described in Section 4.1, see Fig. 17 which provides one realization for each size. Due to the microstructure variability, the volume fraction of each realization deviates from the nominal value of 40% with an error smaller than 5%. A uniaxial tensile
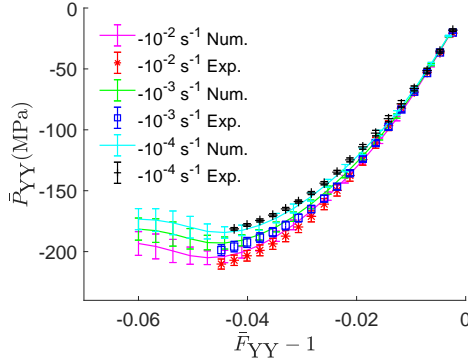
26

Figure 15: Model predictions compared to the experimental results in [8] of composites under uniaxial compressive loading at true strain rates of -10^{-2} s^{-1}, -10^{-3} s^{-1}, and -10^{-4} s^{-1}.
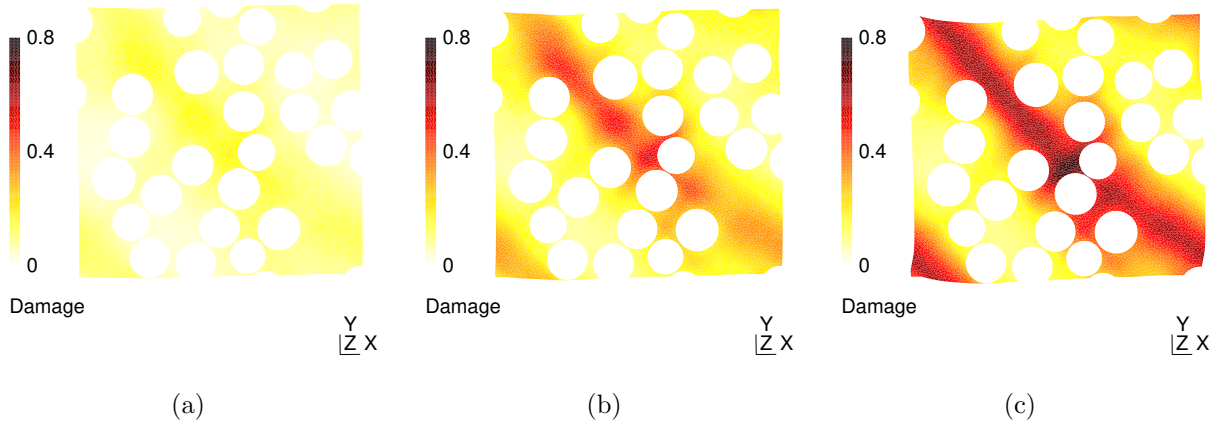

Figure 16: Distribution of the total damage variable D for the SMVE realization illustrated in Fig. 6a: (a) prior to the localization onset, (b) at the onset of localization, and (c) after the onset of localization under constant true strain rates of -10^{-2} s^{-1}.

loading is applied along the vertical Y-direction. Since the numerical model possibly exhibits snapback, the rate-independent case is considered by setting all viscoelastic and viscoplastic material constants to zero. As a result, the path following framework described in Section 3.5 is used to follow the homogenized stress-strain curve from the beginning up to the total failure.

The homogenized responses are shown in Fig. 18a in terms of the homogenized Cauchy stress component $\bar{\sigma}_{YY}$ evolution with the loading component of the deformation gradient $\bar{F}_{YY} - 1$. The difference in the homogenized responses of the different SMVEs increases with the applied deformation. The prepeak response seems to be objective with the SMVE dimension although some discrepancies are observed since the SMVE are not statistically representative. In the post-peak localization stage, the larger the SMVE dimension along the loading direction, the more pronounced the snapback is in the homogenized response. Figure 18b depicts the failure diagrams in terms of the evolution of the homogenized dissipation density, defined as the total dissipation divided by the SMVE volume, as a function of the homogenized Cauchy stress component $\bar{\sigma}_{YY}$. The difference in the responses of the homogenized dissipation density increases during the loading process in accordance with the observations from Fig. 18a. As stated at the beginning of this work, the dissipation accumulated during the post-peak localization stage does not scale with the SMVE volume. Therefore the larger the SMVE volume is, the lower the accumulated dissipation density is.

Although the homogenized stress-strain curves and the failure diagrams in the post-peak localization stage depend on the SMVE sizes, the material strength and critical energy release rate characterizing the
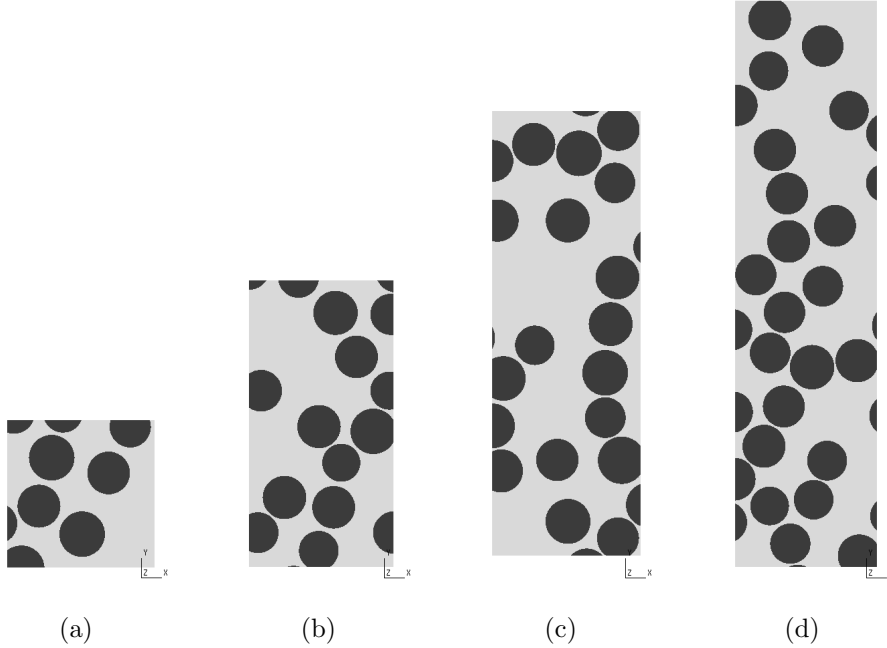
27

Figure 17: A SMVE realization with increasing dimensions: (a) 20 μm×20 μm, (b) 20 μm×40 μm, (c) 20 μm×60 μm, and (d) 20 μm×80 μm.

homogenized cohesive law can be extracted using Eqs. (79, 76). As demonstrated through different studies [2, 3], the objectivity of these homogenized quantities with respect to the SMVE dimensions is recovered. Since the distribution of fibers in different realizations of SMVEs is not the same, different values of the cohesive strength and of the critical energy release rate are extracted. The numerical results of the cohesive strength and of the critical energy release rate are shown in Figs. 19a and b, respectively, in terms of the average values and their deviations. Only a slight sensitivity of the average values of these two parameters with the SMVE size is observed, that supports their SMVE size independence. Both parameters have a wide deviation for the different realizations of the same size. Since only 10 realizations are considered for each SMVE size, the real discrepancy of these material characteristics is not correctly captured: more realizations and varying the SMVE width would be required to conduct a statistical analysis.

Figures 20 and 21 show respectively the distribution of the total damage variable D at peak stress and at total failure for the SMVE realizations illustrated in Fig. 17. The damage localization bands are perpendicular to the loading direction in accordance with literature, see *e.g.* [7, 3]. By the fact that the interfaces between fibers and matrix are not considered, the failure of composites occurs by the failure of the matrix region close to the fibers. It is also observed that the damage localizes in regions where the fibers are closely packed because of the high stress concentration developing in the fibers ligaments. As a result, the fibers ligament distance is an important factor controlling the failure behavior of the unidirectional composites under transverse loading, which justifies the use of statistical indicator to generate the micro-structures [9].

6. Conclusion

The present work provides an efficient virtual testing facility for composites based on a nonlinear computational micromechanics model.

The numerical simulations are performed with SMVEs generated using the statistical information of a real microstructure with a highly irregular dispersion of fibers. A viscoelastic-viscoplastic-damage model accounting for the pressure dependency and strain rate effects is used to model the matrix bahvior. This
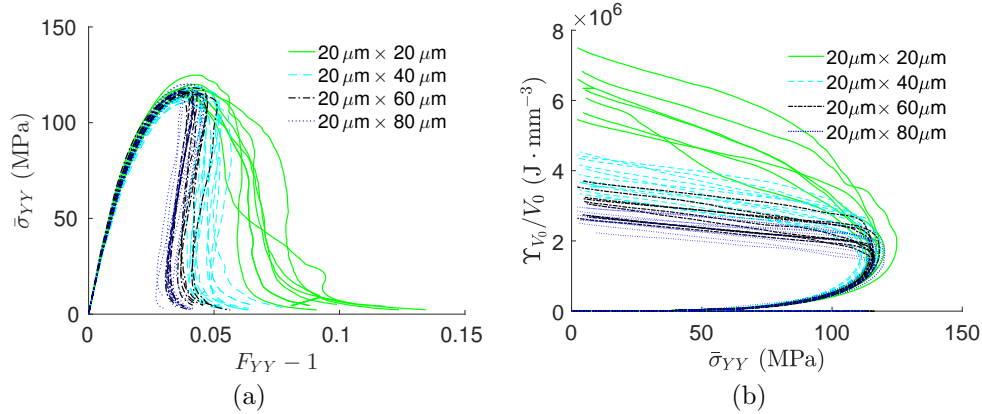
28

Figure 18: Evolution of homogenized quantities: (a) homogenized stress component $\bar{\sigma}_{YY}$ as a function of the homogenized strain component $\bar{F}_{YY} - 1$ and (b) homogenized dissipation density Υ_{V_0}/V_0 as a function of the homogenized stress component $\bar{\sigma}_{YY}$.
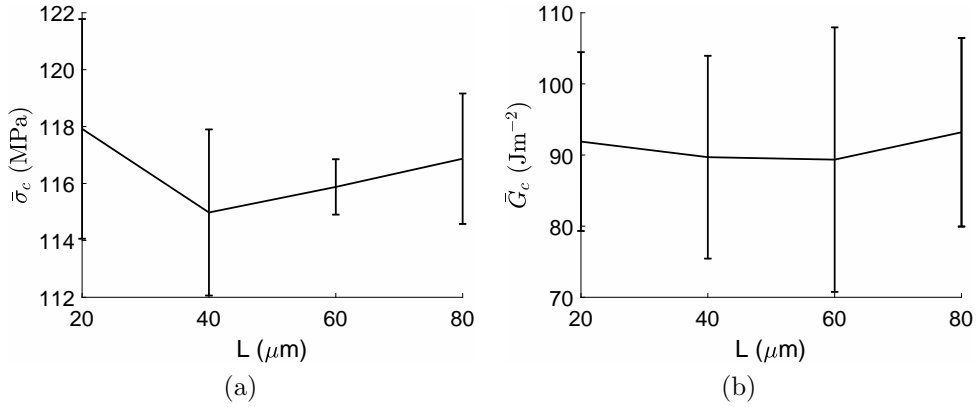

Figure 19: Extraction of cohesive parameters: (a) cohesive strength $\bar{\sigma}_c$ and (b) critical energy release rate $\bar{G}_c$ as functions of the SMVE size. Average values and their deviations are reported.

model is enhanced by multi-mechanism nonlocal damage variables to model post-peak softening and failure. At fibers/matrix interfaces, the isolation condition is considered for the nonlocal failure plasticity variable and the balance condition is used for nonlocal saturation plasticity variable in order to correctly capture the interaction between the fibers and the matrix.

Size effects are incorporated in this constitutive model through the nonlocal length scales, which allow capturing, in good agreement with the experimental results, the behavior of the pure matrix and of the composite material in terms of the global stress-strain curves over various strain rates.

Under monotonic loading applied to the composites, the homogenized stress-strain behavior starts with a linear elastic stage followed by a prepeak nonlinear stage; after that the post-peak stage lasts until the total failure. When the size of the SMVEs increases, a snapback possibly occurs. This kind of behavior is captured using the path following method based on the dissipation increment. This finite element resolution is applied to study the material strength and critical energy release rates of composites under uniaxial tensile loading with a sequence of SMVEs of increasing sizes. These failure characteristics are found to be objective to the SMVEs size despite of the existence of wide deviations due to the randomness in the microstructures. Although matrix/fiber decohesion is not considered for the composites under investigation, the failure of the matrix is observed to occur close to the fibers. In the regions with highly packed fibers, the stress concentration is more pronounced. Therefore, the distance of the fibers ligaments is one of the most important factors that affects the failure behavior of the composites. Since only a small number of
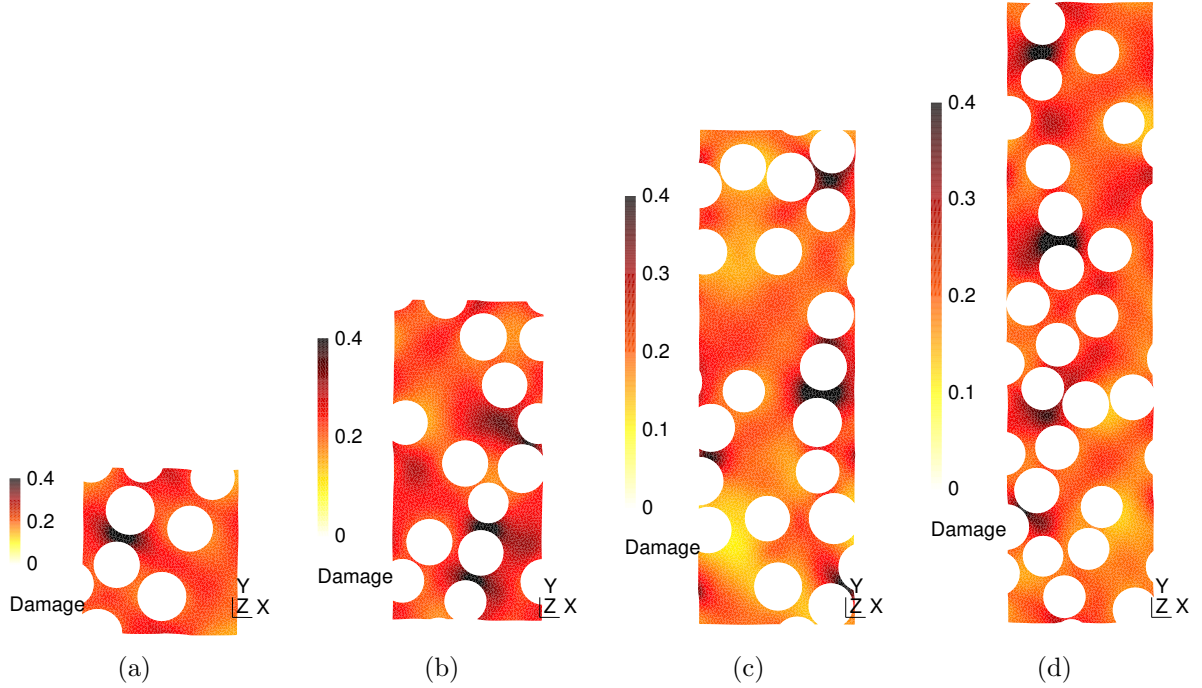
Figure 20: Distributions of the total damage variable D in the matrix at peak stress of SMVE realizations illustrated in Fig. 17: (a) 20 µm×20 µm, (b) 20 µm×40 µm, (c) 20 µm×60 µm, and (d) 20 µm×80 µm.

realizations is considered for each SMVE size, the real discrepancy of these material characteristics is not correctly captured. In a future work, a more extended statistical study will be conducted using this current framework.

Acknowledgment

Appendix A. Virtual testing strategy

The response of structures made of dissipative solids generally follows an irreversible equilibrium path, which is characterized by an increase of the dissipated energy. In this section, the resolution of the weak form (50) follows the path following technique based on the increase of the dissipated energy. This modeling strategy is detailed in this section.

Appendix A.1. Homogenized deformation gradient driven by control nodes

First, $\bar{\mathbf{F}}$ is eliminated from the system of equation (50) using the displacements of the control nodes 1, 2, and 4, see Fig. 2 for their positions. The periodicity constraint of the displacement field leads to

$$\begin{cases} \dot{\mathbf{u}}_2 - \dot{\mathbf{u}}_1 = \dot{\bar{\mathbf{F}}} \cdot (\mathbf{X}_2 - \mathbf{X}_1) \;, \dot{\mathbf{u}}_4 - \dot{\mathbf{u}}_1 = \dot{\bar{\mathbf{F}}} \cdot (\mathbf{X}_4 - \mathbf{X}_1) \;, \end{cases} \tag{A.1}$$
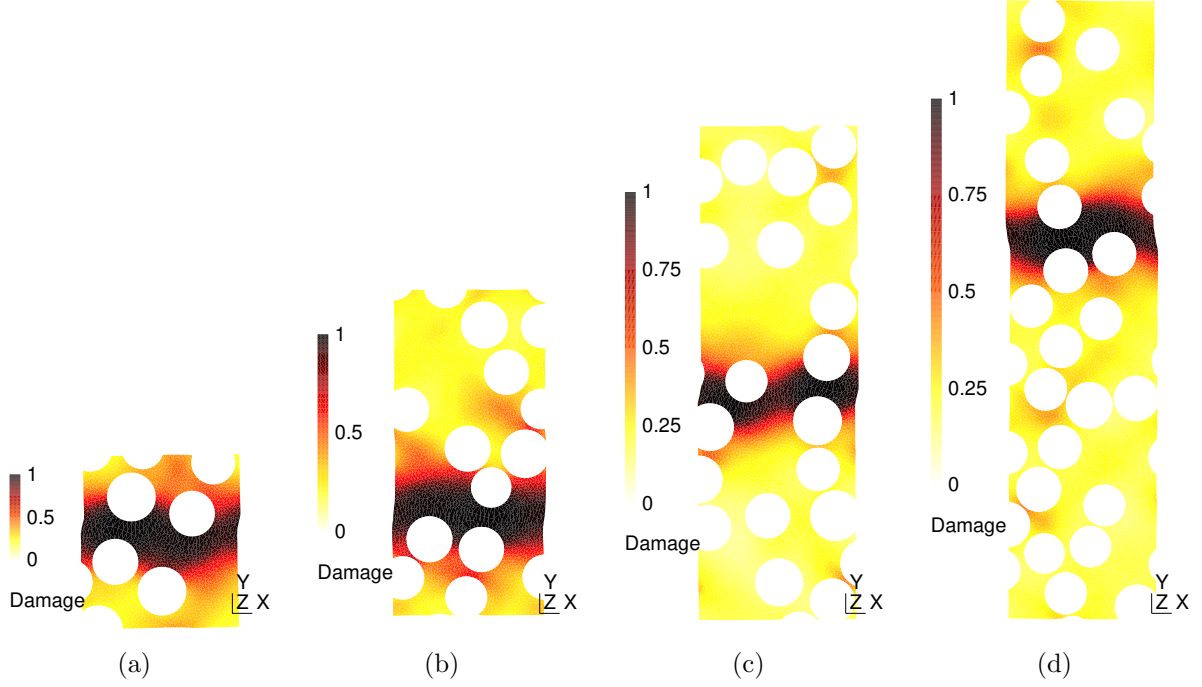
Figure 21: Distribution of the total damage variable D in the matrix at final failure of SMVE realizations illustrated in Fig. 17: (a) 20 μm×20 μm, (b) 20 μm×40 μm, (c) 20 μm×60 μm, and (d) 20 μm×80 μm.

from which, the homogenized deformation gradient $\bar{\mathbf{F}}$ is expressed as

$$\dot{\bar{\mathbf{F}}} = \frac{(\dot{\mathbf{u}}_2 - \dot{\mathbf{u}}_1) \otimes \mathbf{N}_R}{|\mathbf{X}_2 - \mathbf{X}_1|} + \frac{(\dot{\mathbf{u}}_4 - \dot{\mathbf{u}}_1) \otimes \mathbf{N}_T}{|\mathbf{X}_4 - \mathbf{X}_1|} \,, \tag{A.2}$$

where $\mathbf{N}_R = \frac{\mathbf{X}_2 - \mathbf{X}_1}{|\mathbf{X}_2 - \mathbf{X}_1|}$ and $\mathbf{N}_T = \frac{\mathbf{X}_4 - \mathbf{X}_1}{|\mathbf{X}_4 - \mathbf{X}_1|}$.

Appendix A.2. Weak form

The external power performed over the SMVE is given by the right hand side of the Hill-Mandel condition (49), which is expressed using Eq. (A.2) as

$$\bar{\mathbf{P}} : \dot{\bar{\mathbf{F}}} = \mathbf{f}_1^{ext} \cdot \dot{\mathbf{u}}_1 + \mathbf{f}_2^{ext} \cdot \dot{\mathbf{u}}_2 + \mathbf{f}_4^{ext} \cdot \dot{\mathbf{u}}_4 \,, \tag{A.3}$$

where $\mathbf{f}_1^{ext}$, $\mathbf{f}_2^{ext}$, and $\mathbf{f}_4^{ext}$ are the external force vectors exerted at the control nodes and given by

$$\begin{cases} \mathbf{f}_1^{ext} = -\frac{\bar{\mathbf{P}} \cdot \mathbf{N}_R}{|\mathbf{X}_2 - \mathbf{X}_1|} - \frac{\bar{\mathbf{P}} \cdot \mathbf{N}_T}{|\mathbf{X}_4 - \mathbf{X}_1|} \,, \\ \mathbf{f}_2^{ext} = \frac{\bar{\mathbf{P}} \cdot \mathbf{N}_R}{|\mathbf{X}_2 - \mathbf{X}_1|} \,, \\ \mathbf{f}_4^{ext} = \frac{\bar{\mathbf{P}} \cdot \mathbf{N}_T}{|\mathbf{X}_4 - \mathbf{X}_1|} \,. \end{cases} \tag{A.4}$$

Using the external power given in Eq. (A.3), the weak form (50) is rewritten as

$$\begin{cases} \langle \mathbf{P} : (\dot{\mathbf{u}} \otimes \boldsymbol{\nabla}_0) \rangle_{V_0} - (\mathbf{f}_1^{ext} \cdot \dot{\mathbf{u}}_1 + \mathbf{f}_2^{ext} \cdot \dot{\mathbf{u}}_2 + \mathbf{f}_4^{ext} \cdot \dot{\mathbf{u}}_4) = 0 \,, \\ \langle (\bar{\gamma} - \gamma) \dot{\bar{\gamma}} + c_s \boldsymbol{\nabla}_0 \bar{\gamma} \cdot \boldsymbol{\nabla}_0 \dot{\bar{\gamma}} \rangle_{V_0} = 0 \,, \\ \langle (\bar{\gamma}_f - \gamma_f) \dot{\bar{\gamma}}_f + c_f \boldsymbol{\nabla}_0 \bar{\gamma}_f \cdot \boldsymbol{\nabla}_0 \dot{\bar{\gamma}}_f \rangle_{V_0} = 0 \,. \end{cases} \tag{A.5}$$

The SMVE domain V_0 is discretized into finite elements such that $V_0 = \bigcup_e \Omega_0^e$. The test and trial functions are defined over an element Ω_0^e in terms of the standard interpolation concept

$$\begin{cases} \mathbf{q}\left(\mathbf{X} \in \Omega_0^e\right) & = \mathbf{N}^e\left(\mathbf{X}\right) \mathbf{q}^e \\ \dot{\mathbf{q}}\left(\mathbf{X} \in \Omega_0^e\right) & = \mathbf{N}^e\left(\mathbf{X}\right) \dot{\mathbf{q}}^e \end{cases} \text{ over } \Omega_0^e, \tag{A.6}$$

where $\mathbf{q}^e$ denotes the unknown vector over Ω_0^e, and where $\mathbf{N}^e$ is a matrix consisting of the shape functions. With the use of the finite element approximation expressed in Eq. (A.6), the weak form (A.5) yields the following discrete nonlinear equation

$$\dot{\mathbf{Q}}\left(\mathbf{F}^{int} - \mathbf{F}^{ext}\right) = 0, \tag{A.7}$$

where $\mathbf{F}^{int}$ and $\mathbf{F}^{ext}$ are respectively internal and external force vectors, and where $\mathbf{Q}$ is the unknown vector including both displacement and nonlocal unknowns.

Appendix A.3. Multiple constraint resolution

By replacing the homogenized deformation gradient $\bar{\mathbf{F}}$ in the kinematic constraints (57) by the one expressed in Eq. (A.2), one has

$$\begin{cases} \dot{\mathbf{u}}\left(\mathbf{X}^-\right) & = \sum_{i=1}^N \mathbb{N}_i\left(\mathbf{X}^-\right) \dot{\mathbf{v}}^i, \\ \dot{\mathbf{u}}\left(\mathbf{X}^+\right) & = \sum_{i=1}^N \mathbb{N}_i\left(\mathbf{X}^-\right) \dot{\mathbf{v}}^i + \left(\dot{\mathbf{u}}_2 - \dot{\mathbf{u}}_1\right) \frac{\mathbf{N}_R \cdot \left(\mathbf{X}^+ - \mathbf{X}^-\right)}{|\mathbf{X}_2 - \mathbf{X}_1|} + \left(\dot{\mathbf{u}}_4 - \dot{\mathbf{u}}_1\right) \frac{\mathbf{N}_T \cdot \left(\mathbf{X}^+ - \mathbf{X}^-\right)}{|\mathbf{X}_4 - \mathbf{X}_1|}. \end{cases} \tag{A.8}$$

As there is no void at the boundary of the SMVE, the finite element interpolation over ∂V_0^- can be considered as the interpolation form $\mathbb{N}_i$.

Combining these constraints to the finite element discretization (A.7) of the SMVE leads to a multi-point linear constraints system [24]. Following [24], the microscopic boundary condition following Eq. (A.8) can be expressed under the matrix form

$$\mathbf{C}_b \mathbf{Q}_b = \mathbf{0}, \tag{A.9}$$

where $\mathbf{C}_b$ is the constraint matrix, see [24] for its detailed expressions depending on the considered microscopic boundary condition, and where $\mathbf{Q}_b$ is the constrained unknowns vector.

Equations (A.7, A.9) must be simultaneously resolved. In this work, the resolution strategy follows the constraints elimination method proposed in [24], leading to

$$\mathbb{T}^T\left(\mathbf{F}^{int} - \mathbf{F}^{ext}\right) = \mathbf{0}, \tag{A.10}$$

where $\mathbb{T}$ is the constraint elimination matrix which is constructed from $\mathbf{C}_b$, see [24] for details.

Appendix A.4. Path following technique based on dissipated energy

The nonlinear Eqs. (A.10) can be generally resolved by means of an incremental Newton-Raphson iterative procedure by introducing a scalar λ, so-called load factor, such that

$$\mathbf{F}^{ext} = \lambda \hat{\mathbf{F}}^{ext}, \tag{A.11}$$

where $\hat{\mathbf{F}}^{ext}$ is the reference load vector which is estimated at the beginning of the simulation. The nonlinear problem stated by the system of Eqs. (A.10) cannot generally converge in one iteration, therefore the external loading must be divided into increments until reaching the final value (*e.g.* $\lambda = 1$). Under a pure load control (unknown, force or their combination), the load factor λ is prescribed by a monotonically increasing function. However, a pure force control fails after the peak load as the structure cannot support any positive load increment, while a pure unknown control cannot be used to follow the snapback behavior since the load factor must decrease to hold the equilibrium path. These problems can be addressed using a path following

technique, in which λ is considered as an extra unknown in order to follow an arbitrary equilibrium path. Therefore, an additional constraint, so-called path-following constraint, must be considered to complete the problem statement. This constraint can be given under a general form

$$\Phi\left(\mathbf{U}, \mathbf{U}_n, \lambda, \lambda_n; \mathbf{Z}, \mathbf{Z}_n\right) - \tau = 0\,, \tag{A.12}$$

where $\mathbf{Z}$ is a vector including all the internal variables; where the subscript n stands for a value obtained at the previous converged solution; and where τ is the prescribed path following step.

The residual of the equilibrium system of equations (A.10, A.12) is defined as

$$\mathbf{R} = \begin{bmatrix} \mathbb{T}^T\left(\mathbf{F}^{int} - \lambda\hat{\mathbf{F}}^{ext}\right) \\ \Phi - \tau \end{bmatrix} = \begin{bmatrix} \mathbf{0} \\ 0 \end{bmatrix}\,. \tag{A.13}$$

From $(\mathbf{U}_n, \lambda_n)$, which is the converged solution of the system of equations (A.13) at time t_n, the system state at time t_{n+1} and at iteration i is denoted by $\left(\mathbf{U}_{n+1}^{(i)}, \lambda_{n+1}^{(i)}\right)$, in which $\mathbf{U}_{n+1}^{(0)} = \mathbf{U}_n$ and $\lambda_{n+1}^{(0)} = \lambda_n$ are known. The resolution at iteration $i+1$ follows the linearized equations

$$\mathbf{R}^{i+1} = \mathbf{R}^i + \begin{bmatrix} \mathbb{T}^T\mathbf{K}\mathbb{T} & -\mathbf{f} \\ \mathbf{g}^T & h \end{bmatrix} \begin{bmatrix} \mathbf{U}_{n+1}^{(i+1)} - \mathbf{U}_{n+1}^{(i)} \\ \lambda_{n+1}^{(i+1)} - \lambda_{n+1}^{(i)} \end{bmatrix} = \begin{bmatrix} \mathbf{0} \\ 0 \end{bmatrix}\,, \tag{A.14}$$

where the sub-matrices are given by

$$\mathbf{K} = \frac{\partial\mathbf{F}_{int}}{\partial\mathbf{U}}\,, \mathbf{f} = \mathbb{T}^T\hat{\mathbf{F}}_{ext}\,, \mathbf{g} = \frac{\partial\Phi}{\partial\mathbf{U}}\,, \text{ and } h = \frac{\partial\Phi}{\partial\lambda}\,. \tag{A.15}$$

We note that the system (A.14) only involves the stiffness matrix of the microscopic finite element discretization, and not an homogenized material tensor. Its resolution leads to

$$\begin{bmatrix} \mathbf{U}_{n+1}^{(i+1)} \\ \lambda_{n+1}^{(i+1)} \end{bmatrix} = \begin{bmatrix} \mathbf{U}_{n+1}^{(i)} \\ \lambda_{n+1}^{(i)} \end{bmatrix} - \begin{bmatrix} \mathbb{T}^T\mathbf{K}\mathbb{T} & -\mathbf{f} \\ \mathbf{g}^T & h \end{bmatrix}^{-1} \mathbf{R}^i\,. \tag{A.16}$$

The iteration process continues until satisfying a convergence condition. Two criteria must be simultaneously considered: the one from the unbalance in the forces, and the other one from the path following constraint, i.e.

$$\max\left(\frac{\left\|\mathbb{T}^T\mathbf{F}^{int} - \lambda\mathbb{T}^T\hat{\mathbf{F}}^{ext}\right\|}{\left\|\mathbb{T}^T\mathbf{F}^{int}\right\| + |\lambda|\left\|\mathbb{T}^T\hat{\mathbf{F}}^{ext}\right\|}, \frac{|\Phi|}{|\tau|}\right) < \varepsilon\,, \tag{A.17}$$

where ε is the prescribed tolerance.

The path following framework described above is valid for any arbitrary path following constraint. In this work, this path following constraint is constructed from the dissipated energy evolution as considered in [15]. The path following is only applicable in case of rate independent material laws since the load value at the boundary is also an unknown of the problem; the viscosity effects in the matrix cannot considered. When the dissipated energy is not always increasing, e.g. during elastic responses, this strategy must be coupled with another control type [15]. The easiest way is to couple with a pure load control such as

$$\Phi = \Delta\lambda - \tau_l = 0\,, \tag{A.18}$$

where τ_l is the prescribed load increment. After the onset of the irreversible regime characterized by $\dot{\Upsilon}_{V_0} > 0$, the path following constraint can be switched to a dissipating regime by directly constraining the amount

of the dissipated energy per step $\tau_{\mathcal{D}}$ as

$$\Phi = \Delta \Upsilon_{V_0} - \tau_{\mathcal{D}} = 0 \,, \tag{A.19}$$

where the increment operator Δ is defined in comparison with the previous converged solution. The condition (A.19) constrains the irreversible equilibrium path to be traced. Clearly, an analysis always starts with a pure load condition following Eq. (A.18), which can be switched to the dissipated energy-based control following Eq. (A.19) after the onset of the irreversible state. The proposed framework requires two parameters: load factor and dissipated energy increments to trace the equilibrium path.

Appendix B. Dimensionless analysis

The dependency of the critical energy release rate G_c on the nonlocal length l can be eliminated using a dimensionless analysis with l considered as the reference length of the problem.

Considering the setup illustrated in Fig. 11a, one can define dimensionless length and dimensionless radius as

$$\bar{L}_0 = \frac{L_0}{l} \text{ and } \bar{R}_0 = \frac{R_0}{l} \,, \tag{B.1}$$

and Eq. (66) is rewritten as

$$\Upsilon_{V_0}(t) = l^3 \bar{\Upsilon}_{\bar{V}_0}(t) \sigma_c \tag{B.2}$$

where $\bar{\Upsilon}_{\bar{V}_0}$ is the dimensionless dissipation, which is given by

$$\bar{\Upsilon}_{\bar{V}_0}(t) = \frac{1}{\sigma_c} \int_0^t \int_{\bar{V}_0} \dot{\mathcal{D}}_m \, d\bar{V} \, dt \,. \tag{B.3}$$

In this relation $\bar{V}_0$ is the dimensionless volume defined by $\bar{L}_0$ and $\bar{R}_0$, and σ_c is the material strength, which is estimated from the evolution of the true stress across the cylinder following Eq. (86), as

$$\sigma_c = \max\left[\sigma(t) \,; t \in [0 \,\infty)\right] \,. \tag{B.4}$$

Using Eq. (B.2), Eq. (85) leads to

$$G_c = \bar{G}_c l \sigma_c \,, \tag{B.5}$$

where $\bar{G}_c$ is the dimensionless critical energy release rate

$$\bar{G}_c = \frac{\bar{\Upsilon}_{\bar{V}_0}^{\text{end}} - \bar{\Upsilon}_{\bar{V}_0}^{\text{loc}}}{\pi \bar{R}_0^2} \,. \tag{B.6}$$

Clearly, $\bar{G}_c$ depends only on the material parameters and on the geometry of the problem but not on the nonlocal parameter l, such that

$$\bar{G}_c = \bar{G}_c \left(\bar{L}_0, \bar{R}_0, \chi_{fc}\right) \,. \tag{B.7}$$

Figures B.22a and b show the influence of $\bar{L}_0$ when fixing $\bar{R}_0 = 1$ and $\chi_{fc} = 0.1$. The numerical response does not depend on $\bar{L}_0$ when its value if larger than 1. Therefore, the value of L_0 can be arbitrary chosen larger than 1. The influence of $\bar{R}_0$ when fixing $\bar{L}_0 = 10$ and $\chi_{fc} = 0.1$ is depicted in Figs. B.23a and b. Although the stress-strain curves in terms of the true stress as a function of the radius reduction depend on $\bar{R}_0$, $\bar{G}_c$ seems to be not sensitive to $\bar{R}_0$ if this value is small enough. From Figs. B.22a and b and Figs.
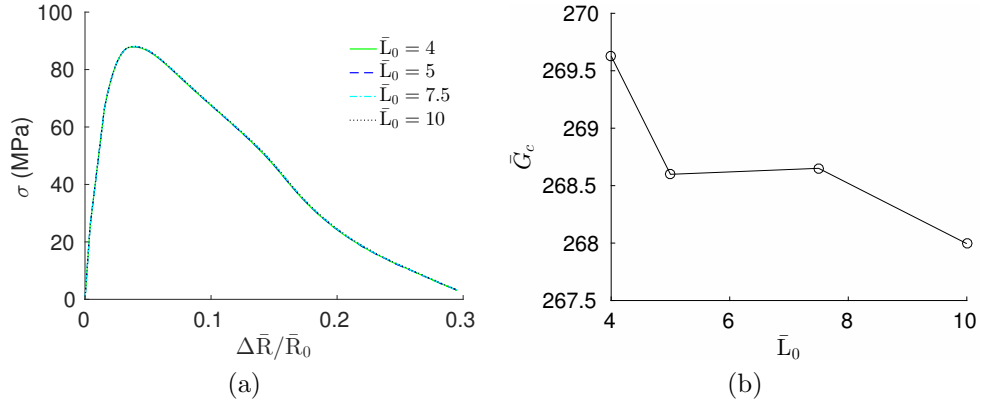
Figure B.22: Influence of $\bar{L}_0$ at constant $\bar{R}_0 = 1$ and constant $\chi_{fc} = 0.1$: (a) stress- strain curve and (b) estimated $\bar{G}_c$.
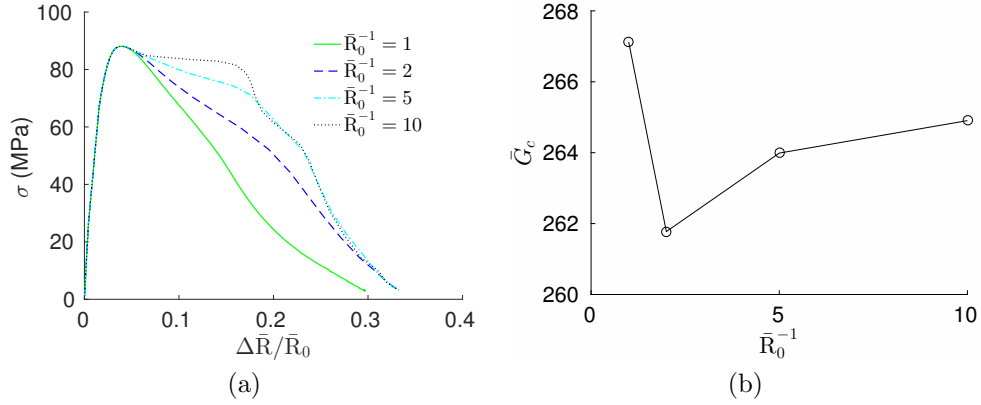

Figure B.23: Influence of $\bar{R}_0$ at constant $\bar{L}_0 = 10$ and constant $\chi_{fc} = 0.1$: (a) stress- strain curve and (b) estimated $\bar{G}_c$

B.23a and b, one can choose $\bar{L}_0 \gg 1$ and $\bar{R}_0 \ll 1$ from which Eq. (B.7) is rewritten in the simpler form

$$\bar{G}_c = \bar{G}_c \left(\chi_{fc} \right) . \tag{B.8}$$

References

[1] K. Matou, M. G. Geers, V. G. Kouznetsova, A. Gillman, A review of predictive nonlinear theories for multiscale modeling of heterogeneous materials, Journal of Computational Physics 330 (2017) 192 – 220. `doi:https://doi.org/10.1016/j.jcp.2016.10.070`.
URL `http://www.sciencedirect.com/science/article/pii/S0021999116305782`

[2] V. P. Nguyen, O. Lloberas-Valls, M. Stroeven, L. J. Sluys, On the existence of representative volumes for softening quasi-brittle materials a failure zone averaging scheme, Computer Methods in Applied Mechanics and Engineering 199 (45-48) (2010) 3028 – 3038. `doi:http://dx.doi.org/10.1016/j.cma.2010.06.018`.
URL `http://www.sciencedirect.com/science/article/pii/S0045782510001854`

[3] L. Wu, D. Tjahjanto, G. Becker, A. Makradi, A. Jérusalem, L. Noels, A micromeso-model of intra-laminar fracture in fiber-reinforced composites based on a discontinuous galerkin/cohesive zone method, Engineering Fracture Mechanics 104 (2013) 162 – 183. `doi:http://dx.doi.org/10.1016/j.engfracmech.2013.03.018`.
URL `http://www.sciencedirect.com/science/article/pii/S0013794413001252`

[4] G. Vigueras, F. Sket, C. Samaniego, L. Wu, L. Noels, D. Tjahjanto, E. Casoni, G. Houzeaux, A. Makradi, J. M. Molina-Aldareguia, M. Vzquez, A. Jrusalem, An xfem/czm implementation for massively parallel simulations of composites fracture, Composite Structures 125 (2015) 542 – 557. `doi:https://doi.org/10.1016/j.compstruct.2015.01.053`.
URL `http://www.sciencedirect.com/science/article/pii/S0263822315001063`

[5] D. Xie, A. M. Waas, Discrete cohesive zone model for mixed-mode fracture using finite element analysis, Engineering Fracture Mechanics 73 (13) (2006) 1783 – 1796. `doi:https://doi.org/10.1016/j.engfracmech.2006.03.006`.
URL `http://www.sciencedirect.com/science/article/pii/S0013794406001007`

[6] C. Gonzlez, J. LLorca, Mechanical behavior of unidirectional fiber-reinforced polymers under transverse compression: Microscopic mechanisms and modeling, Composites Science and Technology 67 (13) (2007) 2795 – 2806. `doi:https://doi.org/10.1016/j.compscitech.2007.02.001`.
URL `http://www.sciencedirect.com/science/article/pii/S0266353807000711`

[7] A. Melro, P. Camanho, F. A. Pires, S. Pinho, Micromechanical analysis of polymer composites reinforced by unidirectional fibres: Part ii micromechanical analyses, International Journal of Solids and Structures 50 (11) (2013) 1906 – 1915. `doi:https://doi.org/10.1016/j.ijsolstr.2013.02.007`.
URL `http://www.sciencedirect.com/science/article/pii/S0020768313000723`

[8] J. Chevalier, P. Camanho, F. Lani, T. Pardoen, Multi-scale characterization and modelling of the transverse compression response of unidirectional carbon fiber reinforced epoxy, Composite Structures 209 (2019) 160 – 176. `doi:https://doi.org/10.1016/j.compstruct.2018.10.076`.
URL `http://www.sciencedirect.com/science/article/pii/S0263822318325133`

[9] L. Wu, C. N. Chung, Z. Major, L. Adam, L. Noels, From sem images to elastic responses: A stochastic multiscale analysis of ud fiber reinforced composites, Composite Structures 189 (2018) 206 – 227. `doi:https://doi.org/10.1016/j.compstruct.2018.01.051`.
URL `http://www.sciencedirect.com/science/article/pii/S0263822317327770`

[10] X. P. Morelle, J. Chevalier, C. Bailly, T. Pardoen, F. Lani, Mechanical characterization and modeling of the deformation and failure of the highly crosslinked rtm6 epoxy resin, Mechanics of Time-Dependent Materials 21 (3) (2017) 419–454. `doi:10.1007/s11043-016-9336-6`.
URL `https://doi.org/10.1007/s11043-016-9336-6`

[11] M. R. Gudimetla, I. Doghri, A finite strain thermodynamically-based constitutive framework coupling viscoelasticity and viscoplasticity with application to glassy polymers, International Journal of Plasticity 98 (2017) 197 – 216. `doi:https://doi.org/10.1016/j.ijplas.2017.08.001`.
URL `http://www.sciencedirect.com/science/article/pii/S0749641917301286`

[12] V.-D. Nguyen, F. Lani, T. Pardoen, X. Morelle, L. Noels, A large strain hyperelastic viscoelastic-viscoplastic-damage constitutive model based on a multi-mechanism non-local damage continuum for amorphous glassy polymers, International Journal of Solids and Structures 96 (2016) 192 – 216. `doi:http://dx.doi.org/10.1016/j.ijsolstr.2016.06.008`.
URL `http://www.sciencedirect.com/science/article/pii/S0020768316301238`

[13] A. Melro, P. Camanho, S. Pinho, Generation of random distribution of fibres in long-fibre reinforced composites, Composites Science and Technology 68 (9) (2008) 2092 – 2102. `doi:https://doi.org/10.1016/j.compscitech.2008.03.013`.
URL `http://www.sciencedirect.com/science/article/pii/S0266353808001048`

[14] T. Hobbiebrunken, M. Hojo, T. Adachi, C. D. Jong, B. Fiedler, Evaluation of interfacial strength in cf/epoxies using fem and in-situ experiments, Composites Part A: Applied Science and Manufacturing 37 (12) (2006) 2248 – 2256, the 11th USJapan Conference on Composite Materials. `doi:https://doi.org/10.1016/j.compositesa.2005.12.021`.
URL `http://www.sciencedirect.com/science/article/pii/S1359835X06000066`

[15] S. May, J. Vignollet, R. de Borst, A new arc-length control method based on the rates of the internal and the dissipated energy, Engineering Computations 33 (1) (2016) 100–115. `doi:10.1108/EC-02-2015-0044`.
URL `http://dx.doi.org/10.1108/EC-02-2015-0044`

[16] J. Bonet, A. J. Burton, A simple orthotropic, transversely isotropic hyperelastic constitutive equation for large strain computations, Computer Methods in Applied Mechanics and Engineering 162 (1-4) (1998) 151 – 164. `doi:10.1016/S0045-7825(97)00339-3`.
URL `http://www.sciencedirect.com/science/article/pii/S0045782597003393`

[17] J. Lemaitre, J.-L. Chaboche, Mechanics of solid materials, Cambridge university press, 1994.

[18] P. Perzyna, Thermodynamic theory of viscoplasticity, Vol. 11 of Advances in Applied Mechanics, Elsevier, 1971, pp. 313 – 354. `doi:https://doi.org/10.1016/S0065-2156(08)70345-4`.
URL `http://www.sciencedirect.com/science/article/pii/S0065215608703454`

[19] R. H. J. Peerlings, R. De Borst, W. A. M. Brekelmans, J. H. P. De Vree, Gradient enhanced damage for quasi-brittle materials, International Journal for Numerical Methods in Engineering 39 (19) (1996) 3391–3403.
URL `http://www.scopus.com/inward/record.url?eid=2-s2.0-0030267284&partnerID=tZOtx3y1`

[20] R. Peerlings, T. Massart, M. Geers, A thermodynamically motivated implicit gradient damage framework and its application to brick masonry cracking, Computer Methods in Applied Mechanics and Engineering 193 (3032) (2004) 3403 – 3417, computational Failure Mechanics. `doi:https://doi.org/10.1016/j.cma.2003.10.021`.
URL `http://www.sciencedirect.com/science/article/pii/S0045782504001380`

[21] V.-D. Nguyen, E. Béchet, C. Geuzaine, L. Noels, Imposing periodic boundary condition on arbitrary meshes by polynomial interpolation, Computational Materials Science 55 (0) (2012) 390 – 406. `doi:10.1016/j.commatsci.2011.10.017`.
URL `http://www.sciencedirect.com/science/article/pii/S0927025611005866`

[22] E. Coenen, V. Kouznetsova, M. Geers, Novel boundary conditions for strain localization analyses in microstructural volume elements, International Journal for Numerical Methods in Engineering 90 (1) (2012) 1–21. `doi:10.1002/nme.3298`.
URL `http://dx.doi.org/10.1002/nme.3298`

[23] S. D. Mesarovic, J. Padbidri, Minimal kinematic boundary conditions for simulations of disordered microstructures, Philosophical Magazine 85 (1) (2005) 65–78. `doi:10.1080/14786430412331313321`.

[24] V.-D. Nguyen, L. Wu, L. Noels, Unified treatment of microscopic boundary conditions and efficient algorithms for estimating tangent operators of the homogenized behavior in the computational homogenization method, Computational Mechanics 59 (3) (2017) 483–505. `doi:10.1007/s00466-016-1358-z`.
URL `https://doi.org/10.1007/s00466-016-1358-z`

[25] V. P. Nguyen, O. Lloberas-Valls, M. Stroeven, L. J. Sluys, Computational homogenization for multiscale crack modeling. implementational and computational aspects, International Journal for Numerical Methods in Engineering 89 (2) (2012) 192–226. `doi:10.1002/nme.3237`.
URL `http://dx.doi.org/10.1002/nme.3237`

[26] L. H. Poh, G. Sun, Localizing gradient damage model with decreasing interactions, International Journal for Numerical Methods in Engineering 110 (6) (2017) 503–522. `arXiv:https://onlinelibrary.wiley.com/doi/pdf/10.1002/nme.5364`, `doi:10.1002/nme.5364`.
URL `https://onlinelibrary.wiley.com/doi/abs/10.1002/nme.5364`

[27] J. Chevalier, X. Morelle, P. Camanho, F. Lani, T. Pardoen, On a unique fracture micromechanism for highly cross-linked epoxy resins, Journal of the Mechanics and Physics of Solids 122 (2019) 502 – 519. `doi:https://doi.org/10.1016/j.jmps.2018.09.028`.
URL `http://www.sciencedirect.com/science/article/pii/S0022509618303545`